

Horizon replicas in black hole shadows

D. Pugliese¹ and H. Quevedo^{2*}

¹ *Research Centre for Theoretical Physics and Astrophysics,
Institute of Physics, Silesian University in Opava,
Bezručovo náměstí 13, CZ-74601 Opava, Czech Republic*

² *Instituto de Ciencias Nucleares, Universidad Nacional Autónoma de México, AP 70543, México, DF 04510, Mexico
Dipartimento di Fisica and ICRA, Università di Roma "La Sapienza", I-00185 Roma, Italy*

(Dated: October 1, 2024)

Recently, new exploratory channels have opened up for the physics of highly compact objects, such as gravitational waves and black hole shadows. Moreover, more precise analysis and observations are now possible in the physics of accretion around compact objects. These advancements provide in particular an unprecedented insight into the physics near the horizons of a black hole. In this work we focus on the shadow boundary of a Kerr black hole, introducing observables related to special null orbits, called horizons replicas, solutions of the shadow edge equations which are related to particular photon orbits, defined by constraints on their impact parameter, carrying information about the angular momentum of the central spinning object. These orbits are related to particular regions on the shadow boundary and might be used to determine the spin of the black hole. The results provide the conditions by which horizon replicas are imprinted in the black hole shadow profile, in dependence on the black hole dimensionless spin and observational angle, providing eventually new templates for the future observations.

I. INTRODUCTION

In this work, we study some aspects of black hole (**BH**) shadow boundary (edge/critical curve) related to special null orbits called horizons replicas, characterized by impact parameter (specific angular momentum) $\ell = \ell_H^\pm(a)$ equal in magnitude to the angular momentum of the outer and inner **BH** horizons, respectively (a is the **BH** dimensionless spin). The analysis introduces new observables related to replicas and discussing the relation with the **BH** spin and its inclination angle with the respect to an observer at infinity.

The observation of the close proximity of the **BH** horizon (**BH** shadow) located at the center of the giant elliptical galaxy **M87** by the **Event Horizon Telescope (EHT)** Collaboration¹ constitutes a consistent advance in observational astronomy, allowing a tight interplay between theoretical analysis and the observations—see [1–8] (and [9] for a recent sharper image of the **M87 BH**, created with PRIMO algorithm). More recently the **EHT** Collaboration has been able to observe also the shadow, as asymmetric rings of synchrotron emissions, cast by the super-massive **BH (SMBH)** Sagittarius **A*** (**SgrA***), located at the center of our galaxy [10–15].

The **EHT** observations, provide in particular a new insight in the physical phenomena in the close proximity of the **BH** event horizon. On the other hand, **BHs** shadows have been studied extensively analytically—see for example [16–19]—where we should note that main notion of the **BH** shadow refers mostly to the shadow edge (the shadow luminous boundary), rather than the shadow itself, being the dark region bounded by the luminous edge, constituted by unstable (spherical and circular) photon orbits—[16–19, 21–24]. In many analysis the **BH**, assumed embedded in a luminous environment, is considered located before the screen and the distant observer. The photons, moving towards the **BH**, could be trapped in unstable circular orbits, and can reach the far away observer after perturbation. Photons could escape to infinity and detected by the distant observer in light of sight, or they can be captured by the central **BH** generating the **BH** shadow as the central dark region. The **BH** shadow profile (luminous edge) can be also affected by the matter environment and could depend also on properties of the region of the light distribution and its source².

However, in all cases, the shadow profile morphology reflects the **BH** parameters, which can be estimated by the analysis of observable related to the topological and morphological properties of the shadow boundary curve, constructed for example, using special points on the shadow boundary in the celestial coordinates (α, β) (see also [20–24]). These observables for a Kerr **BH** carry information on the central spinning attractor and the photon orbits

* daniela.pugliese@physics.slu.cz, quevedo@nucleares.unam.mx

¹ <https://eventhorizontelescope.org>.

² In these conditions, the photons could interact with the accreting plasma modifying both photons distribution and the intensity—see for example [25–31].

constituting the luminous texture of the boundary. In this work, we assume that photons are generated by a distant source at infinity and are distributed uniformly in *all* directions, observers are also located at infinity, and that the Kerr **BH** has a well defined and fixed³ inclination angle θ , which is defined by the angle between the **BH** rotation axis and the observer line of sight.

In general, the **BH** shadow profile is found considering photons having *all* the possible values of the impact parameters ℓ , therefore solving the equations for the shadow profile, system (\mathfrak{R}) , for *all* values of ℓ . In our analysis, we solve (\mathfrak{R}) in dependence on the **BH** dimensionless spin $a \in [0, 1]$ and of the observational θ angle, constraining assuming $\ell = \pm \ell_H^\pm(a)$, for co-rotating and counter-rotating motion (determined by the ℓ parameter). By solving (\mathfrak{R}) , within the constraints $\ell = \pm \ell_H^\pm(a)$, we examine the parts of the luminous edges (shadows profiles) associated to the null geodesics at fixed constraints, mapping in this way the **BH** luminous edges in dependence of the selected values for ℓ . The investigation explores all possible values of $a \in [0, 1]$ and $\theta \in [0, \pi/2]$. The results provide the constrained celestial coordinate (β, α) for different θ and for different spins. In this way we relate the photons, within the constraints considered in these analysis, to the observation coordinates (α, β) (that is the location on the shadow profile), the observation angle θ and the **BH** spin, distinguishing points on the **BHs** shadow profiles correspondent to the fixed constraints. The collections of all the points, for fixed constraints, for all values of the observational angles define curves in the plane (α, β) we study in our analysis.

The quantity $\ell_H^\pm(a)$, constraining photons in the **BH** shadow profile, are also the basis for the definition of replicas⁴. The Kerr **BH** events horizons are Killing horizons of \mathcal{L}_H^\pm , where $\mathcal{L}_H^\pm \equiv \xi_{(t)} + \omega_H^\pm \xi_{(\phi)}$, ω_H^\pm is the angular velocity (frequency) of the outer and inner horizons, respectively, $(\xi_{(t)}, \xi_{(\phi)})$ are the Killing vectors of the Kerr metric, associated with time translations and rotations along the angle ϕ . There is $\ell_H^\pm(a) = 1/\omega_H^\pm$. The horizons degenerate at $r = M$ for extreme Kerr **BHs**, where the angular frequency is $\omega_H^\pm = 1/2$ for a static observer at infinity. Replicas are photon orbits whose constant parameter $\ell \equiv 1/\omega$ is, in magnitude, ℓ_H^+ or ℓ_H^- . The set of all photon (circular) orbits with equal fixed ω , constitutes an object called metric Killing bundles (or simply metric bundles), with characteristic frequency ω , which is always a **BH** horizon frequency^[32–38]. Only some replicas are solutions of system (\mathfrak{R}) and will appear consequently on the luminous texture of the shadow boundary.

Future observational advancements and new data analysis techniques will allow more clear observation and description of the **BH** environment, discerning more refined structure of the images. There is indeed a continuous improvement (and updating) of the images. For example, combining data from radio telescopes Global Millimetre VLBI Array, ALMA, and the Greenland Telescope, the ring-like accretion structure in **M87** has been shown connecting the **BH** plasma jet to the **BH** and the accretion matter ^[39]. On the other hand a new analysis of **EHT** data, using a PRIMO algorithm, sharpened the earlier view of the glowing gas around the **M87 BH** ^[9]. In ^[40] again the **M87*** images from **EHT** collaboration has been re-analyzed, using a series of kinetic plasma simulations, predicting the images during the outbursts characterizing **M87***. New analysis also provides evidence of a rotating jet ejected from the **BH** region –see also ^[41] and ^[9, 20, 41–46]. (Then, in ^[43], revisiting the past observations, it has been claimed to have spotted the sharp light ring around **M87***—see also ^[9, 41, 42, 44, 47–49]).

Therefore we expect that it will be possible to observe more refined and clearer details from the astronomical observations in near future (see ^[39]) and the features proposed in this work, related to horizon **BH** replicas, could be used as a guiding idea for future observational enhancements where the regions highlighted here will be distinctly recognizable.

This article is structured as follows:

In Sec. (II), we introduce the spacetime metric and the equations of motion. Constants of motion and geodesic equations are presented in Sec. (II A). The main aspects of black hole shadows are discussed in Sec. (III). The constants of motion q and ℓ are investigated in Sec. (III A). The celestial coordinates (α, β) , which define the shadow boundary, are introduced in Sec. (III B). In Sec. (III C) we discuss the constraint adopted in our analysis. In Sec. (IV) starts the analysis of the **BH** shadow equations within condition $\ell = \mp \ell_H^\pm$.

We proceed solving equations (\mathfrak{R}) within the constraints on the impact parameter $\ell = \mp \ell_H^\pm$. Hence, in Sec. (IV A), we solve (\mathfrak{R}) with $\ell = \pm \ell_H^\pm$ for the radius r and the Carter constant q , and in Sec. (IV B) we discuss the celestial

³ A further interesting aspect would be to investigate **BH** shadows following a spin variation (precession) process.

⁴ The quantity $\ell_H^\pm(a)$ turns out to be significant for the study of **BH** physics, in particular, to investigate its interaction with the environment and its consequent evolution. It is a well known fact that limits of **BH** energy extraction are imposed by the **BH** horizon. Indeed, massive particles or photons with momentum p^μ that cross the outer horizon r_+ of a Kerr **BH** should satisfy the inequality $-p_\mu (\mathcal{L}_H^\pm)^\mu \geq 0$. This implies that $\mathcal{E} - \omega_H^\pm \mathcal{L} \geq 0$, for $\mathcal{E} \equiv -p_\mu \xi_{(t)}^\mu$ (energy), where $\mathcal{L} = p_\mu \xi_{(\phi)}^\mu$ is the ϕ component of the particle (photon) angular momentum. Thus, $\ell \equiv \mathcal{L}/\mathcal{E} \leq \ell_H^\pm \equiv 1/\omega_H^\pm$. If the energy \mathcal{E} is negative, \mathcal{L} is negative and the **BH** spin is reduced, (**BH** spin–down). The process is regulated by $\delta J/\delta M \leq \ell_H$ (where J is the Kerr **BH** spin and M its mass, δ is for the variation) regulating also the super-irradiance as the analogue Penrose process for radiation scattering by a Kerr **BH**. For a wave–mode of angular-frequency ω , ω is amplified if $\omega \in]0, z/\ell_H^\pm[$, where $z \in Z - \{0\}$ is the wave angular momentum number.

coordinates (α, β) for the replicas on the shadow profile. (Further details are also discussed in Appendix (B)). Concluding remarks are given in Sec. (V). Two Appendix sections follow. More notes on the concept and formalism of metric bundles are in Sec. (A): in Sec. (A1) the concept of metric bundles and replicas is deepened. Relations between definition of photon circular orbits and replicas are discussed in Sec. (A2). Sec. (A2a) clarifies the relation between concepts of photons spheres and replicas. In Sec. (A2b) we relate circular photons orbits and replicas. Sec. (B) contain details on shadow analysis of Sec. (IV A).

II. THE SPACETIME METRIC

The Kerr spacetime metric reads

$$ds^2 = - \left(1 - \frac{2Mr}{\Sigma} \right) dt^2 + \frac{\Sigma}{\Delta} dr^2 + \Sigma d\theta^2 + \left[(r^2 + a^2) + \frac{2Mra^2}{\Sigma} \sin^2 \theta \right] \sin^2 \theta d\phi^2 - \frac{4rMa}{\Sigma} \sin^2 \theta dt d\phi, \quad (1)$$

in the Boyer-Lindquist (BL) coordinates $\{t, r, \theta, \phi\}$ ⁵, where

$$\Delta \equiv a^2 + r^2 - 2rM \quad \text{and} \quad \Sigma \equiv a^2 \cos^2 \theta + r^2. \quad (2)$$

The parameter $a = J/M \geq 0$ is the metric spin, where the total angular momentum is J and the gravitational mass parameter is M . A Kerr **BH** is defined by the condition $a \in [0, M]$ with inner and outer Killing horizons $r_- \leq r_+$ respectively, where $r_{\pm} \equiv M \pm \sqrt{M^2 - a^2}$. The extreme Kerr **BH** has dimensionless spin $a/M = 1$ and the non-rotating case $a = 0$ corresponds to the Schwarzschild **BH** solution. The Kerr naked singularities (**NSs**) have $a > M$.

For further analyses it is convenient to introduce the angular parameter $\sigma \equiv \sin^2 \theta \in [0, 1]$. The equatorial plane, $\sigma = 1$, is a metric symmetry plane and the equatorial circular geodesics are confined to the equatorial plane as a consequence of the metric tensor symmetry under reflections with respect to the plane $\theta = \pi/2$. The outer ergoregion of the spacetime is $]r_+, r_{\epsilon}^+]$, where the outer stationary limit r_{ϵ}^+ (outer ergosurface) is

$$r_{\epsilon}^+ \equiv M + \sqrt{M^2 - a^2(1 - \sigma)}, \quad (3)$$

where $r_{\epsilon}^+ = 2M$ on the equatorial plane $\theta = \pi/2$ ($\sigma = 1$), and $r_+ < r_{\epsilon}^+$ on $\theta \neq 0$.

In the following analyses, we will use dimensionless units with $M = 1$ (equivalent to $r \rightarrow r/M$ and $a \rightarrow a/M$).

A. Constants of motion and geodesic equations

We consider the following constants of motion

$$\mathcal{E} = -(g_{t\phi}\dot{\phi} + g_{tt}\dot{t}), \quad \mathcal{L} = g_{\phi\phi}\dot{\phi} + g_{t\phi}\dot{t}, \quad g_{ab}u^a u^b = \kappa\mu^2, \quad (4)$$

which are associated with the rotational Killing field $\xi_{(\phi)} \equiv \partial_{\phi}$ and the Killing field $\xi_{(t)} \equiv \partial_t$, representing the stationarity of the background. Moreover, $u^a \equiv \{\dot{t}, \dot{r}, \dot{\theta}, \dot{\phi}\}$, where a dot stands for the derivative with respect to the proper time (for $\mu > 0$) or, in the case of lightlike geodesics, to a properly defined affine parameter (for $\mu = 0$). Finally, $\kappa = (\pm, 0)$ is a normalization constant with $\kappa = -1$ for massive particles. The constant \mathcal{L} in Eq. (4) may be interpreted as the axial component of the angular momentum of a test particle following timelike geodesics and \mathcal{E} represents the total energy of the test particle, as measured by a static observer at infinity.

We introduce also the specific angular momentum [18, 19]

$$\ell \equiv \frac{\mathcal{L}}{\mathcal{E}} = -\frac{g_{\phi\phi}u^{\phi} + g_{\phi t}u^t}{g_{tt}u^t + g_{\phi t}u^{\phi}} = -\frac{g_{t\phi} + g_{\phi\phi}\omega}{g_{tt} + g_{t\phi}\omega}, \quad (5)$$

where $\omega \equiv u^{\phi}/u^t$ is the relativistic angular velocity, related to the parameter ℓ as follows

$$\omega(\ell) = -\frac{g_{t\phi} + g_{tt}\ell}{g_{\phi\phi} + g_{t\phi}\ell}. \quad (6)$$

⁵ We adopt the geometrical units $c = 1 = G$ and the $(-, +, +, +)$ signature, Latin indices run in $\{0, 1, 2, 3\}$. The radius r has unit of mass $[M]$, and the angular momentum units of $[M]^2$, the velocities $[u^t] = [u^r] = 1$ and $[u^{\theta}] = [u^{\phi}] = [M]^{-1}$ with $[u^{\phi}/u^t] = [M]^{-1}$ and $[u_{\phi}/u_t] = [M]$.

In the following we consider co-rotation or counter-rotation according to the condition $a\ell \gtrless 0$ respectively. The geodesic equations in the Kerr spacetime are fully separable and define four constants of motion. For convenience we summarize the (Carter) equations of motion as follows [50]:

$$\dot{t} = \frac{1}{\Sigma} \left[\frac{P(a^2 + r^2)}{\Delta} - a[a\mathcal{E}(\sin\theta)^2 - \mathcal{L}] \right], \quad \dot{r} = \pm \frac{\sqrt{R}}{\Sigma}; \quad \dot{\theta} = \pm \frac{\sqrt{T}}{\Sigma}, \quad \dot{\phi} = \frac{1}{\Sigma} \left[\frac{aP}{\Delta} - \left[a\mathcal{E} - \frac{\mathcal{L}}{(\sin\theta)^2} \right] \right], \quad (7)$$

where

$$P \equiv \mathcal{E}(a^2 + r^2) - a\mathcal{L}, \quad R \equiv P^2 - \Delta[(\mathcal{L} - a\mathcal{E})^2 + \mu^2 r^2 + \mathcal{Q}], \quad T \equiv \mathcal{Q} - (\cos\theta)^2 \left[a^2(\mu^2 - \mathcal{E}^2) + \left(\frac{\mathcal{L}}{\sin\theta} \right)^2 \right] \quad (8)$$

and

$$\mathcal{Q} = (\cos\theta)^2 \left[a^2(\mu^2 - \mathcal{E}^2) + \left(\frac{\mathcal{L}}{\sin\theta} \right)^2 \right] + (g_{\theta\theta}\dot{\theta})^2 \quad (9)$$

is the Carter constant.

III. SHADOWS

In this section, we introduce the concept of **BH** shadows. A description of the constants of motion (q, ℓ) is presented in Sec. (III A). The celestial coordinates (α, β) are discussed in Sec. (III B). In Sec. (III C) we discuss the constraints adopted in our analysis.

A. The quantities (q, ℓ)

According to the null geodesic equations (7), the boundary (edge, or luminous edge) of the **BH** shadow, as described by [18], is determined by the (unstable) photon orbits defined by⁶

$$R = \partial_r R = 0, \quad \partial_r^2 R > 0 \quad (10)$$

(hereafter referred as set \mathfrak{R}) of equations), with constraints provided by the set of Eqs. (7) (in particular the condition $T \geq 0$). Following the usual procedure, we introduce the two impact parameters

$$\ell \equiv \frac{\mathcal{L}}{\mathcal{E}}, \quad q \equiv \frac{\mathcal{Q}}{\mathcal{E}^2}. \quad (11)$$

for an observer located at infinity, where photons arrive close to the equatorial plane. Using Eqs (10), we can find the impact parameters (ℓ, q) , independently of σ . Clearly, the condition $(R = 0, R' = 0)$ for $a = 0$ and $q = 0$ corresponds to $(r = 3, \ell = \pm 3\sqrt{3})$, that is, the last lightlike circular orbit on the equatorial plane of the Schwarzschild spacetime, where $R'' > 0$.

B. The celestial coordinates (α, β)

Let us introduce the celestial coordinates α and β as follows [18]:

$$\alpha \equiv \lim_{r_o \rightarrow +\infty} \left(-r_o^2 \sin\theta_o \frac{d\phi}{dr} \Big|_o \right), \quad \beta \equiv \lim_{r_o \rightarrow +\infty} \left(r_o^2 \frac{d\theta}{dr} \Big|_o \right). \quad (12)$$

We assume that the observer is at infinity and r_o is the distance from the central attractor to the position of the observer (r is the ‘‘emission’’ point), θ_o is the inclination angle (the angular coordinate of the distant observer θ_0

⁶ In this work, we also consider solution $\partial_r^2 R = 0$. Note that R does not depend explicitly on σ .

is the inclination angle between the line of sight of the distant observer and the axis of rotation of the central gravitating object). Therefore, α and β are the apparent perpendicular distances of the shadow, as seen from the axis of symmetry, and its projection on the equatorial plane, respectively. The parameters (α, β) are also called the horizontal and vertical impact parameters respectively and are, therefore, evaluated with respect to the point of view of an observer located at infinity. In the following, for simplicity, the subindex o in (r_o, θ_o) will be dropped.

Using Eqs (7) for null geodesics in Eqs (12), we obtain:

$$\beta = \pm\sqrt{q - q_c} \quad \text{for } \sigma \neq 0 \quad \text{and} \quad q \geq q_c, \quad \text{where} \quad q_c \equiv \frac{(\sigma - 1)(a^2\sigma - \ell^2)}{\sigma}, \quad (13)$$

where $\sigma \neq 0$ and in particular for $\sigma = 1$, there is $\beta = \pm\sqrt{q}$.

The quantity β is independent of the rotation orientation (sign of ℓ sign) and of the inclination angle orientation (it is even on θ). For $\sigma = 0$ (attractor poles), this quantity is not well defined. On the equatorial plane, it has to be $q \geq 0$. The sign of β depends on the sign of $(\dot{\theta}, \dot{r})$ in Eqs (12).

The coordinate α satisfies the relationship

$$\alpha = -\frac{\ell}{\sin\theta}, \quad \text{and} \quad \alpha = -\ell \quad \text{for} \quad \theta = \frac{\pi}{2}. \quad (14)$$

Note that α depends on the sign of ℓ , is odd in θ , and does not depend on the attractor spin. We will use definition Eq. (14) in the form $\alpha = -\ell/\sqrt{\sigma}$, which is equivalent to considering $\theta \in [0, 2\pi]$, using the coordinates $(\alpha, -\alpha)$. Then, $\alpha = 0$ for $\ell = 0$.

In the analysis of shadows, we shall consider the function $\beta(\alpha)$.

The quantities (q, r) do not depend on the angle σ . However, the coordinates with respect to the observer at infinity (α, β) depend on σ .

C. Constraints

In this section we introduce the constraints adopted in our analysis, for the set (\mathfrak{R}) of Eq. (10). **BH** shadow profile is in general found, at fixed spin and observational angle, considering photons coming from *all* the points at infinity, having *all* the possible values of the impact parameters ℓ , therefore solving (\mathfrak{R}) for *all* values of ℓ .

We study solutions of the equations (\mathfrak{R}) in dependence on $a \in [0, 1]$ and of the θ angle, within the constraint $\ell = \pm\ell_H^\pm(a)$. That is $|\ell|$ is evaluated on the **BH** outer and inner horizons with $\ell_H^\pm(a) = 1/\omega_H^\pm(a)$, where ω_H^\pm is the angular velocity (frequency) of the horizons, representing the **BH** rigid rotation. Functions $\ell_H^\pm(a)$ are shown in Figs (1)–*left panel* as function of the **BH** spin a . Therefore, counter-rotating and co-rotating photons with $\ell = \pm\ell_H^\pm(a)$ are considered for all possible values of $a \in [0, 1]$ and $\sigma \in [0, 1]$ ($\theta \in [0, \pi/2]$). Hence, these special null circular orbits, characterized by specific angular momentum $\ell = \pm\ell_H^\pm$, i.e. equal in magnitude to the angular momentum of the outer or inner **BH** horizons, have been called counter-rotating or co-rotating, outer or inner, horizons replicas (replicas), [32–38]. The results for (\mathfrak{R}) with $\pm\ell_H^\pm(a)$ provide the constrained celestial coordinate (β, α) , for different θ and for different spins a , distinguishing parts, points or regions, of the luminous edges (shadows profiles) associated to the fixed constraints, i.e. the analysis of solutions (\mathfrak{R}) for $\pm\ell_H^\pm(a)$ individuates particular replicas that appear on the luminous profile of the shadow contour. Solutions with the constraints $\ell = \pm\ell_H^\pm$ are points on the shadow edge and introduce new observable related to the replicas. Horizons replicas can be applied to extract information about the **BH** and, particularly, the **BH** horizons, by measuring properties of the **BH** horizons in regions accessible to distant observers [33, 36]. It has been proved in [32–38] there are Kerr inner horizons replicas in regions very close to the **BH** rotational axis. Therefore, one of the intriguing applications of replicas in **BH** physics is the possibility to explore the regions close to the **BH** rotational axis in order to obtain information about the horizons⁷. While replicas reveal their significance in particular in the region proximal to $\theta \approx 0$ (the **BH** poles) where they are more numerous–[32–38],

⁷ From the phenomenological view point, an observer can detect the presence of a replica at the point p of the **BH** spacetime with spin a , by measuring the **BH** horizon frequency $\omega_H^+(a)$ or $\omega_H^-(a)$ (the outer or inner **BH** horizon frequency) at the point p [36]. It has been pointed out that **MBs** appear to be related to the concept of spacetime *pre-horizon regimes*, indicating the existence of detectable mechanical effects allowing circular orbit observers to recognize the close presence of an event horizon. Pre-horizon regimes were introduced in [51–53]. An implication of this property is that an object like a gyroscope could observe a connected phenomenon and interpret it as a *memory* of the static (Schwarzschild-like) case in the Kerr metric–[57]. Moreover, these structures could play an important role for the description of the black hole formation and for testing the possible existence of naked singularities and could be of relevance during the gravitational collapse [54–56, 58]. Interpretations of similar related concepts have been presented also in [59–61].

in general the existence of replicas is dependent on the **BH** spin a , the radius r and the angle θ . Replicas, like the critical curve, are a characteristic of spacetime only, depending exclusively on the dimensionless **BH** spin, therefore they can be considered to describe the characteristics of the central **BH** from the luminous profile. Since the replicas we consider here are *also* solutions of the equations (\mathfrak{R}), this implies that, at fixed spin a and observational angle σ , they appear as points or regions on the luminous boundary of the **BH** shadow, constituting the luminous texture of the shadow boundary profile⁸. These orbits having same ℓ in absolute value as the **BH** horizons allow to map the critical curve (the shadow edge), by connecting a specific value of the photon impact parameter to certain regions of the shadow contour curve, the radius and Carter constant (r, q) and observational angle θ .

Notes on replicas and Killing metric bundles

While the quantity ℓ_H^\pm is an important **BH** feature limiting for example **BH** energy extraction, we introduce here the constraints $\ell = \pm\ell_H^\pm(a)$ for the system (\mathfrak{R}), as related to the concept of Killing metric bundles (**MBs**)[\[32–38\]](#).

In general **MBs** are defined from the more general Killing field $\mathcal{L}_\omega \equiv \xi_{(t)} + \omega\xi_{(\phi)}$, where $(\xi_{(t)} \equiv \partial_t, \xi_{(\phi)} \equiv \partial_\phi)$ are metric Killing field, defining the quantity $\mathcal{L}_\mathcal{N} \equiv \mathcal{L}_\omega \cdot \mathcal{L}_\omega$, null for photon-like particles with particular rotational frequencies $\omega = \omega_\pm$ (ω_H^\pm are frequencies ω_\pm evaluated on the **BH** horizons r_\pm , this point is discussed more extensively in [Sec. \(A 1\)](#)). Therefore **MBs** are solutions of $\mathcal{L}_\mathcal{N} = 0$, under certain conditions as $\omega = \text{constant}$ or $\ell = \text{constant}$, where $\mathcal{L}_H^\pm = \xi_{(t)} + \omega_H^\pm \xi_{(\phi)}$, and the *angular momentum* $\ell_H^\pm \equiv 1/\omega_H^\pm$. In this analysis we look for those particular solutions that are also solutions of (\mathfrak{R}).

In general, the set of all solutions $\mathcal{L}_\mathcal{N}$ with *equal fixed* orbital ω (bundle characteristic frequency), constitutes a metric Killing bundle (or simply metric bundle). Constant ω turns to be always a **BH** horizon frequency, hence bundle orbits are, in general, all replicas of a **BH** horizon. (Example of replicas on the equatorial plane of Kerr **BH** with spin $a \in [0, 1]$ are discussed in [Sec. \(A 1\)](#)—(see [Eq. \(A 4\)](#) and [Fig. \(10\)](#))). However we are interested here in the case of replicas in a *fixed* Kerr **BH** background. More notes on the concept and formalism of **MBs** are in [Sec. \(A\)](#). In particular, in [Sec. \(A 1\)](#) the concept of metric bundles and replicas is deepened, considering in particular the relation with photon circular geodesic orbits. Relations between definition of photon circular orbits and replicas are discussed in [Sec. \(A 2\)](#). [Sec. \(A 2 a\)](#) clarifies the relation between concepts of photons spheres and replicas. In [Sec. \(A 2 b\)](#) we relate circular photons orbits and replicas.

IV. THE CONDITION $\ell = \epsilon\ell_H^\pm$

We proceed solving equations (\mathfrak{R}) within the constraints on the impact parameter $\ell = \epsilon\ell_H^\pm$, where $\epsilon = \{+1, -1\}$, examining the associated regions on the shadow profiles, in dependence on the **BH** spin and the observational angle. Results provide, for each constraint, the coordinate (β, α) , in dependence of ranges of **BH** spin a , angle σ , and Carter constant q . Constrained photons can be traced on specific regions of the luminous edge and vary depending on the angle of observation and spin. We obtain a relation $\beta(\alpha)$ i.e. we can relate points or regions of the luminous profile (at fixed θ and a) to the fixed constraints. Hence, in [Sec. \(IV A\)](#), we solve (\mathfrak{R}) with $\ell = \epsilon\ell_H^\pm$ for the variables (r, q) , considering the constraints imposed by the Carter equations and in [Sec. \(IV B\)](#) we discuss the celestial coordinates (α, β) for the replicas on the shadow profile. Further details are discussed in [Appendix \(B\)](#).

A. Quantities (q, r) for $\ell = \epsilon\ell_H^\pm$

In this Section we constrain the quantities (q, r) , solutions of (\mathfrak{R}) with $\ell = \epsilon\ell_H^\pm$, for different (a, σ) .

That is we consider the Carter equations for the **BH** shadow profiles with the constraints $\ell = \epsilon\ell_H^\pm$, discussing the results in terms of the quantities (r, q) . By constraining the spin a , regions r , constant q and observational angle θ , results provide, for each constraint on the parameter ℓ , the replicas which are also solutions of the shadow equations (\mathfrak{R}), hence forming the luminous edge solution of (\mathfrak{R}). In [Sec. \(IV B\)](#) we discuss the results in terms of the coordinate celestial coordinates (α, β) .

Let us note there are no solutions of (\mathfrak{R}) ($T > 0$) with $q < 0$ and $R = 0$ (see [Eq. \(13\)](#) and [\(8\)](#)); therefore, there are no solutions for the shadow problem with $q < 0$ so that this condition has to be eliminated from our analysis.

Considering [Eq. \(13\)](#) for $q > 0$, the condition $T \geq 0$ implies $q \geq q_c$, that is, $\sigma \in]0, 1[$ with $\ell^2 < a^2\sigma$ ($q_c < 0$), and $\ell^2 > a^2\sigma$ ($q_c > 0$) with $q > q_c$. Function q_c , evaluated on ℓ_H^\pm is represented in [Figs \(1\)](#)—right panel, as functions of a

⁸ Bundle formalism can easily be related to the solutions of (\mathfrak{R}) in the plane (α, β) in the fact the celestial coordinate α can be directly related to some bundle characteristics (the bundle origin and the bundle tangent spin)—see discussion in [Sec. \(A 1\)](#).

Also, on the equatorial plane $\sigma = 1$ (or for $\ell^2 = a^2\sigma$, i.e., $a^2 = a^2$) we obtain $q_c = 0$ and $q > 0$.

For $q = 0$, from Eq. (13) we obtain that $\sigma = 1$ ($q_c = 0$ and, therefore, also the condition $\ell^2 = a^2\sigma$), or $\sigma \in]0, 1[$ with $\ell^2 < a^2\sigma$ ($q_c < 0$).

From Figs (1)–left panel it is clear that, for any $\sigma \in]0, 1]$, $\ell_H^\pm \in]a\sqrt{\sigma}, \ell_H^\pm]$. (See also Figs (2)–right panel, where celestial coordinate $\alpha \equiv -\ell/\sqrt{\sigma}$ of Eq. (14) is shown as function of the **BH** spin on the equatorial plane and $\ell \in \{\pm\ell_H^-, -\ell_H^+\}$).

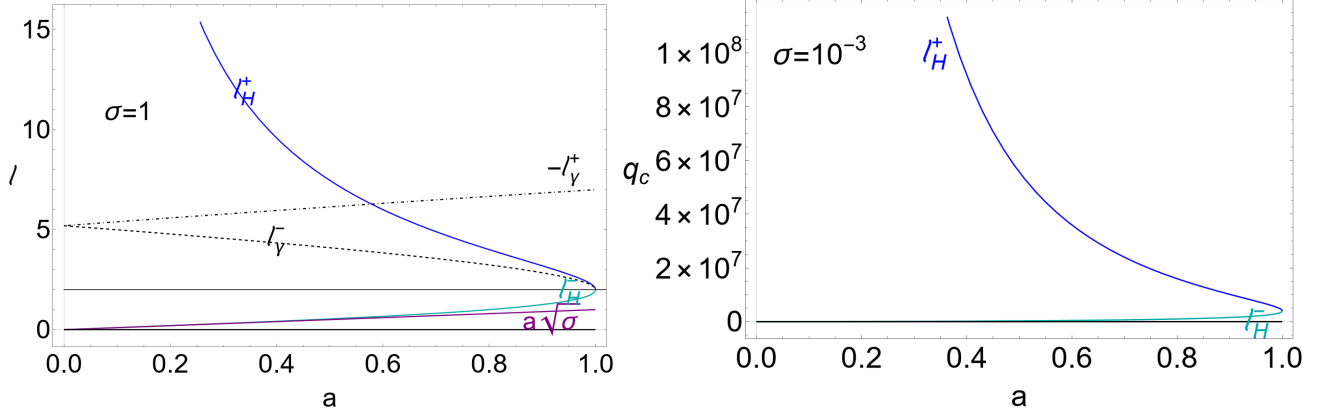


FIG. 1. Left panel: Specific angular momentum $\ell_H^\pm(a)$ of the outer and inner Kerr **BH** horizons, respectively, as functions of the **BH** dimensionless spin a/M and the limiting parameter $\ell = a\sqrt{\sigma}$ (purple line) on the equatorial plane $\sigma \equiv \sin^2\theta = 1$. Radii r_\pm^\pm are the photon counter-rotating and co-rotating circular orbits respectively on the equatorial plane (and boundary of the Kerr **BH** photon sphere—see Sec. (A 2 a)). Right panel: Function q_c of Eq. (13) (q is the Carter constant) for $\sigma = 10^{-3}$ and evaluated for $\ell = \ell_H^\pm(a)$ as function of the **BH** dimensionless spin. All quantities are dimensionless.

Below we discuss in details the results at fixed impact parameter, considering solutions of (\mathfrak{R}) for the cases $\ell = +\ell_H^\pm$ and $\ell = -\ell_H^\pm$ in terms of the constant q and the radius r .

In general (a, r) are related in the solutions of (\mathfrak{R}) as shown in Figs (2)–left panel. Relations (σ, r) and (σ, a) of (\mathfrak{R}) are in Figs (3). Quantity q , solution of the set (\mathfrak{R}) as a function of the **BH** dimensionless spin and of the dimensionless radius r are in Figs (4).

In details, no solutions have been found for the system (\mathfrak{R}) with the constraint $\ell = \ell_H^+(a)$ (co-rotating outer horizon replicas). For $\ell = -\ell_H^+$ (counter-rotating outer horizon replicas) we consider first the solutions of (\mathfrak{R}) for (r, q) . A solution is for $q \equiv q_H^+(r, a)$, where

$$q_H^\pm(r, a) \equiv \frac{r [S_\pm - 8r_\pm(r - 2)]}{a^2\Delta}, \quad \text{where} \quad S_\pm \equiv a^2 \left\{ a^2(r + 2) \pm \left[r(r^2 + 4) + 8\sqrt{1 - a^2} \right] \right\}, \quad (15)$$

for a radius $r_H^+(a) \in]3, r_*^-]$ where $r_*^- \equiv 3.7784$, and $a \in [0, 1]$. (More in general the relations among (a, r, q) are shown for $\ell = -\ell_H^+$ in Figs (4)–solid blue curves.).

In Figs. (2)–left panel, relation (a, r) in the solutions of the equations (\mathfrak{R}) for $\ell = -\ell_H^+$ is represented as spin $a(r) : r = r_H^+(a)$, function of the dimensionless radius r (solid blue curve). Radius r_*^- , bounding r for the extreme Kerr **BH**, is also represented. Radius r_H^+ decreases with the **BH** spin. (Further information is in Sec. (B)).

Therefore, considering null geodetics with $\ell = -\ell_H^+$, and assuming the conditions $(R = 0, R' = 0, R'' \geq 0)$ with $T \geq 0$, we obtain solutions of (\mathfrak{R}) for the extreme Kerr **BH** ($a = 1, r = 3, \sigma \in [\sigma_H^+, 1]$), where the limiting observational angle is $\sigma_H^+ \equiv 2(8 - 3\sqrt{7}) = 0.1255$.

For **BHs** with spin $a \in]a_H^+, 1]$, where $a_H^+ \equiv 0.5785$, there is $\sigma \in [\sigma_\omega^+(a), 1]$ and $r \in]3, r_0^+]$. Finally, for $a = a_H^+$ there are solutions only on the equatorial plane $\sigma = 1$ —see Fig. (3)–right panel. The upper limit on the radius is $r_0^+ \equiv 3.609$ (see Fig. (2)–left panel) and limiting angle σ_ω^+ is shown in Figs (3)–right panel as function of the **BH** dimensionless spin (σ_ω^\pm can be found from Eq. (B3)).

There are solutions of (\mathfrak{R}) for $\ell = -\ell_H^-$ (counter-rotating inner horizon replica) for all **BH** spin $a \in [0, 1]$ with constant $q = q_H^-$ of Eq. (15), and radius $r_H^-(a) \in [r_-, 3]$, where $r_- \equiv 2.87513$ —see⁹ Figs (2)–left panel. More in general

⁹ Radius $r_H^-(a)$ can be found as a zero of the quantity R_H^+ of Eq. (B1).

the quantities (r, q) , for different **BH** spins a , are shown for $\ell = -\ell_H^-$ in Figs (4). Radius r , solution of the equations (\mathfrak{R}) for $\ell = -\ell_H^-$, for all **BH** spin a is shown in Figs. (2)–left panel, as spin function $a(r) : r = r_H^-(a)$, function of the dimensionless radius r (dashed curve). Then, with the conditions $(T \geq 0, R' = 0, R = 0)$, there is a solution of (\mathfrak{R}) in particular for the Schwarzschild **BH** with $(a = 0, \sigma \in]0, 1], r = 3)$, for the Kerr **BH** in $(a \in]0, 1], \sigma \in [\sigma_\omega^-, 1])$, and for the extreme Kerr **BH** with $(a = 1, r = 3, \sigma \in [\sigma_H^+, 1])$, where the limiting angles $(\sigma_\omega^-(a), \sigma_H^+(a))$ are shown in Figs (3)–right panel (and can be found as solutions of Eq. (B3)).

Finally, there are solutions of (\mathfrak{R}) with $\ell = \ell_H^-$ (co-rotating inner horizon replicas) for all for **BH** spin $a \in [0, 1]$ for $q = \bar{q}_H$, with

$$\bar{q}_H \equiv \frac{r [\bar{S} - 8r_-(r - 2)]}{a^2 \Delta} \quad \text{where} \quad \bar{S} \equiv S_+ - 16a^2, \quad (16)$$

and $\bar{r}_H^-(a) \in]1, 3]$ (where the radius $\bar{r}_H^-(a)$ is a zero of the quantity \bar{R}_H^- in Eq. (B4)).

Quantities (a, r, q) in the solutions of (\mathfrak{R}) , for $\ell = \ell_H^-$ are related as in Figs (4)–(blue curves), while in Figs. (2)–left panel, relation (a, r) in the solutions of the equations (\mathfrak{R}) for $\ell = \ell_H^-$ is represented as spin $a(r) : r = \bar{r}_H^-(a)$, function of the dimensionless radius r . In particular, for $\ell = \ell_H^-$, the solutions are $r \in [1, 3]$ and $(r = 3, a = 0, \sigma \in]0, 1])$, and for $r \in]1, 3[$ we obtain $a = \bar{a}_H^-$ (Figs (2)–left panel) with the observational angle bounded in the range $\sigma \in [\sigma_H^-, 1]$,

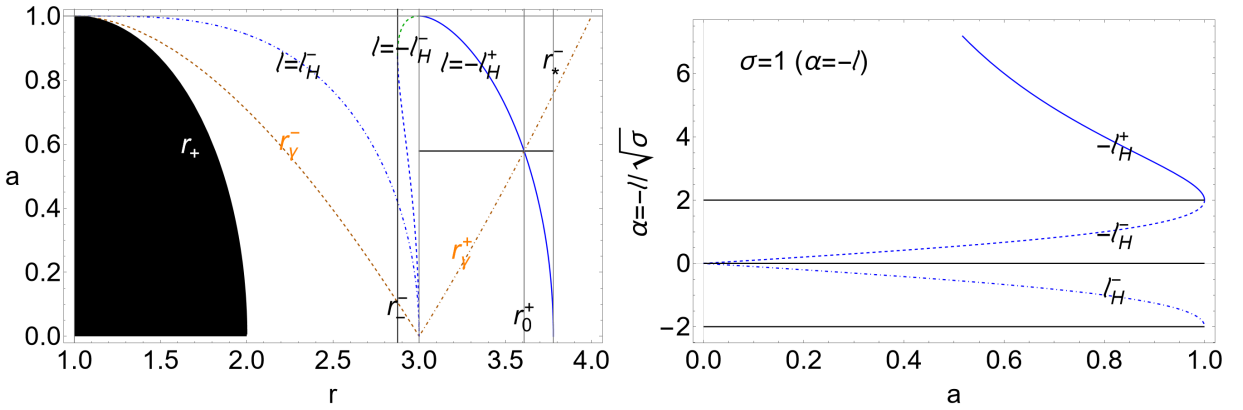


FIG. 2. Left panel: Curves show the relations (a, r) in the solutions of the equations (\mathfrak{R}) of Eq. (10) for $\ell = \pm\ell_H^\pm$. ℓ_H^\pm are the specific angular momenta of the outer and inner Kerr **BH** horizons, respectively. The **BH** region, shown in black, is bounded by the function $a : r = r_+$, where r_+ is the **BH** horizon. Spin function $a(r)$ are function of the dimensionless radius r for $\ell = -\ell_H^+$ (blue solid curve), $\ell = \ell_H^-$ (blue dotted-dashed curve) and $\ell = -\ell_H^-$ (blue dashed curve). Radii $\{r_-, 3, r_0^+, r_*^-\}$ bounding r are also represented. Further discussion on the (r, a) in these cases is also in Sec. (B). Radii r_γ^\pm (orange dotted and dotted-dashed lines) are the photon counter-rotating and co-rotating circular orbits respectively on the equatorial plane (and boundary of the Kerr **BH** photon sphere see Sec. (A 2 a)). Right panel: celestial coordinate $\alpha \equiv -l/\sqrt{\sigma}$ of Eq. (14) as function of the **BH** spin for $\sigma = 1$ (equatorial plane) and $\ell \in \{\pm\ell_H^-, -\ell_H^+\}$. (All quantities are dimensionless.).

where

$$\sigma_H^- \equiv -\frac{2(r\psi + 6)}{(r - 3)\chi}, \quad \text{where} \quad \chi \equiv [(r - 1)r + 2]^2, \quad \psi \equiv [r(3r - 1) + 7]r - 2\sqrt{2}\sqrt{\chi[r(r + 2) + 3]} + 1 \quad (17)$$

–see Figs (3)–left panel.

In Figs (4)–upper panels, q is shown as a function of the **BH** dimensionless spin for $\ell = -\ell_H^+$ and $\ell = \pm\ell_H^-$. The q constant is upper bounded by the value $q = 27$. We analyze, particularly, the case of zero Carter constant ($q = 0$) for $\ell = -\ell_H^+$. This occurs on the background geometry $a = a_H^+$. (The case $q = 0$ reproduces the photon circular orbits on the equatorial plane). The constant q is non negative for $\ell = \pm\ell_H^-$, increases constantly with the spin for $-\ell_H^+$, and decreases with the spin for ℓ_H^- . The situation for $\ell = -\ell_H^-$ is more complex and it is shown in Figs (4)–right panel.

From Figs (4) it can be seen the radial coordinate is, in general, bounded in the range $r \in [1, 3.8]$, i.e., $r \in [1, 3]$ for $\ell = \ell_H^-$, $r \in [r_0^-, 3]$ for $\ell = -\ell_H^-$ (note that in this case there are two values of q for a fixed orbit r –see also Figs (4)), and $r \in [3, r_*^-]$ for $\ell = -\ell_H^+$, where $q = 0$ occurs for $r = r_0^+$. The function $r(a)$ is then shown in Figs (2) as the implicit function $a = a(r)$. For a fixed spin a , it is $r(\ell_H^-) \leq r(-\ell_H^-) \leq r(-\ell_H^+) \in [1, r_*^-]$, where $(r(\pm\ell_H^-), r(-\ell_H^+))$ are the orbits relative to the specific angular momenta $\{\pm\ell_H^-, -\ell_H^+\}$. It is clear there exist two ranges of **BH** spin for $a < a_*$ and $a > a_*$, where $a_* = 0.875473$. Fig. (2) shows also the replica locations with respect to the **BH** outer horizon for different spins. The orbits r are, independently of the plane, close to the **BH** for $r \lesssim 3.8$.

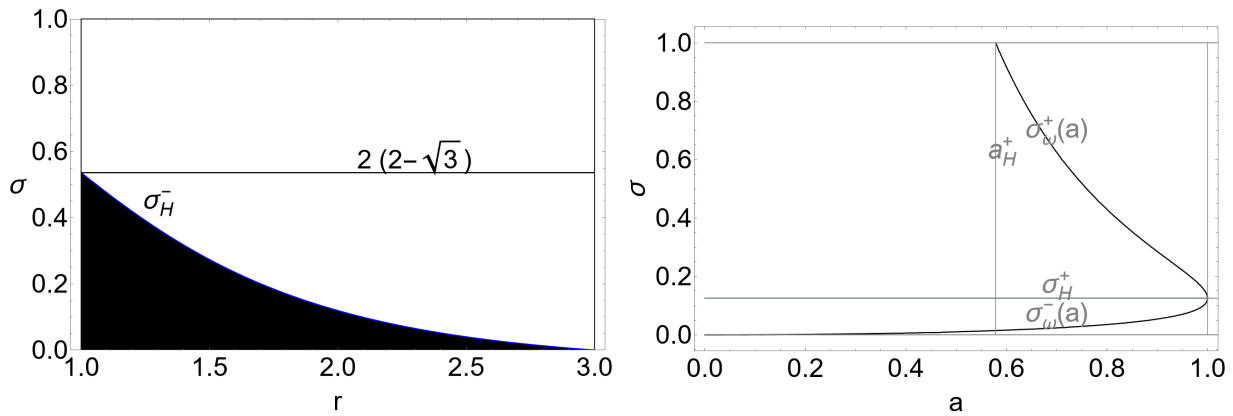


FIG. 3. Relations (σ, r) (left panel) and (σ, a) of the solutions of the equations (\mathfrak{R}) of Eq. (10) for $\ell = \pm\ell_H^\pm$. It follows the discussion of Sec. (IV A). Quantities $\ell_H^\pm(a)$ are the specific angular momenta of the outer and inner Kerr **BH** horizons, respectively, a is the dimensionless **BH** spin, and $\sigma \equiv \sin^2 \theta \in [0, 1]$. Left panel: Plane σ_H^- defined in Eq. (17) as a function of r . Solutions of Eq. (10) for $\ell = \ell_H^-$ exist for $\sigma \in [\sigma_H^-, 1]$. The limiting value $\sigma \approx 0.58$ is also shown. Right panel: Planes σ_ω^\pm , solutions of the equation Eq. (B3), as functions of the **BH** dimensionless spin. Limiting spin a_H^+ is also shown. All quantities are dimensionless.

B. Celestial coordinates (α, β) for the horizons replicas

In this section, we analyze the (α, β) coordinates, solutions of the equations (\mathfrak{R}) , for $\ell = \{\pm\ell_H^-, -\ell_H^+\}$.

Solutions of (\mathfrak{R}) for $\ell = \{\pm\ell_H^-, -\ell_H^+\}$ provide the celestial coordinates (β, α) on the luminous edges, related to the fixed constraints in accordance with spin a , radius r , angle σ and Carter constant q . (Quantities (a, r, σ, q) have been discussed in Sec. (IV A).).

In our analysis, we solve the equations (\mathfrak{R}) (providing the shadow boundary), for null geodesics with $\ell = \pm\ell_H^\pm$ (replicas). Hence we individuate parts of the luminous edges generated by the null geodesics which are *also* replicas, i.e. we consider replicas that can form (and therefore can be observed from) the **BH** shadow boundary, as certain angle θ and for certain spin a . Replicas location on the shadow profiles are then studied for all values of θ and a .

Solutions of this analysis are shown in Figs (5,6) and Figs (7). (Celestial coordinate $\alpha \equiv -\ell/\sqrt{\sigma}$ of Eq. (14) as function of the **BH** spin on the equatorial plane and $\ell \in \{\pm\ell_H^-, -\ell_H^+\}$ is shown in Figs (2)–right panel).

More precisely:

–In Figs (5), the celestial coordinate β , solution of the set (\mathfrak{R}) of Eq. (10) with the constraint $\ell = -\ell_H^+$ (upper panels), $\ell = -\ell_H^-$ (center panels) and $\ell = \ell_H^-$ (bottom panels), is shown as a function of the angular coordinate σ for different values of the spin a signed on the curves (left panels), and in terms of the spin a for different values of σ signed on the curves (right panels). The dotted lines are the limiting values of σ , β , and a .

–In Figs (6), the celestial coordinate β , solution of the set (\mathfrak{R}) of Eq. (10) with the constraint $\ell = -\ell_H^-$ (left panel), for $\ell = \ell_H^-$ (center panel) and for $\ell = -\ell_H^+$ (right panel), is shown as function of α for different **BH** dimensionless spin $a \in [0, 1]$ (solid curves) and angles σ . In these panels, each curve corresponds to a *fixed* spin and a specific constraint, and each point of each curve is for *fixed* σ . Each solid curve is the set of replicas on the **BHs** shadows profiles at fixed **BH** spin a . Each point of a solid curve is a replica for a fixed angle σ . Each dotted curve is the set of replicas on the **BHs** shadows profiles for a fixed plane σ . Each point on a dotted curve is for a specific **BH** spin. Hence, the crossing of the dotted and solid lines, fixes σ and the spin a . Hence, each point (α, β) of a curve provides the corresponding solutions on the **BH** shadow profile.

–In Figs (7) **BH** shadow profiles (celestial coordinate β versus α), solutions of the set (\mathfrak{R}) of Eq. (10) for all values ℓ , are shown for different dimensionless spins $a \in [0, 1]$ and angular coordinate σ (closed black curves). Points corresponding to null geodesic solutions of the set (\mathfrak{R}) within constraints $\ell = \pm\ell_H^\pm$ are vertical lines on the panels. Solving (\mathfrak{R}) with constraints on ℓ , and *fixing* a and σ , we obtain a set of points (α, β) on the shadow profile for the fixed (a, σ) , as shown in Figs (7) (closed curves of Figs (7) obtained at fixed (a, σ) for *all* values of ℓ).

Varying a and σ , we obtained in Figs (5,6) a map of the constrained regions on the shadow profiles, for *all* the observational angles σ and for *all* **BH** spins a .

Solving (\mathfrak{R}) with constraints on ℓ at *fixed* a and for *all* values of the observational angle σ , provides a set of points on the shadow profile representing the superimposition of the points on the shadow boundary relative to the constrained

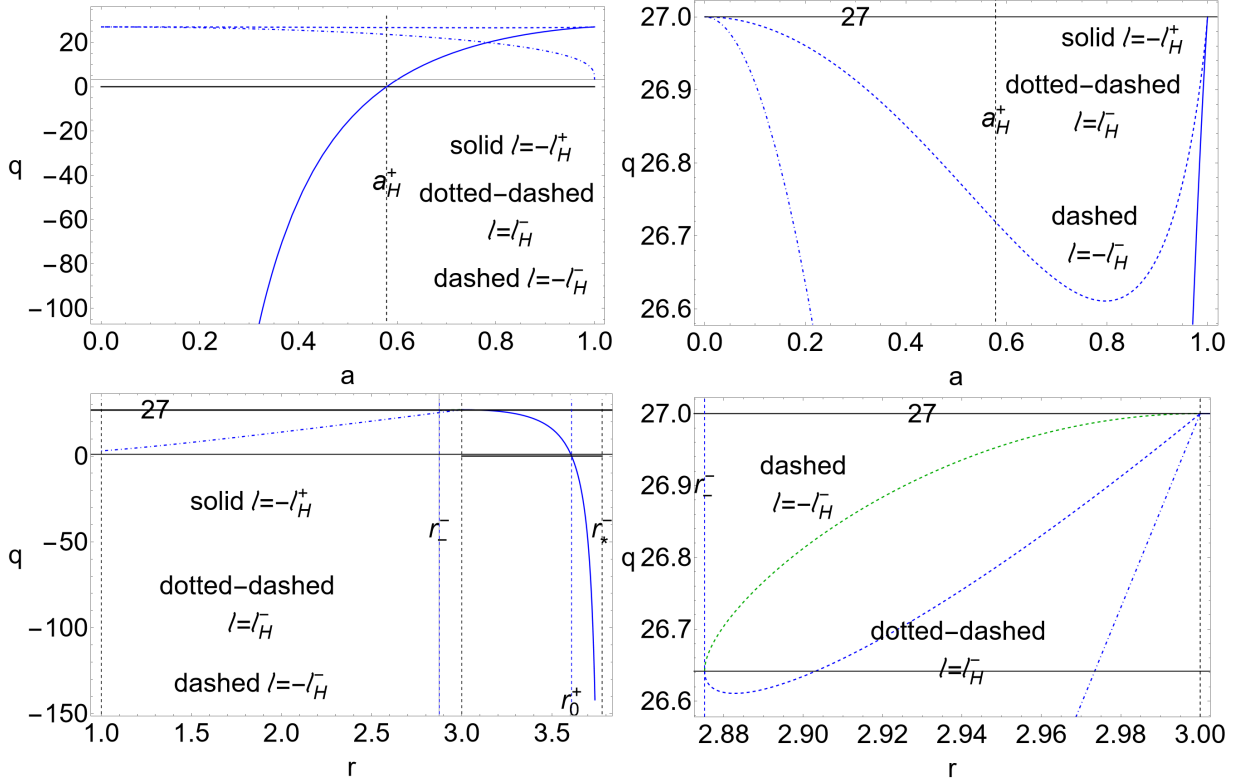


FIG. 4. Quantity q (Carter constant of Eq. (11)) solutions of the set (\mathfrak{R}) of Eq. (10) for $\ell = \pm\ell_H^\pm$ as a function of the **BH** dimensionless spin (upper panels) and as a function of the dimensionless radius r (bottom panels) for $\ell = -\ell_H^+$ (solid curve), $\ell = \ell_H^-$ (dotted-dashed curve) and $\ell = -\ell_H^-$ (dashed curve). Vertical dashed lines are limiting spins and radii. The quantities ℓ_H^\pm are the outer and inner horizons angular momentum, respectively. The right panels are a close-up view of the left panels. The zeros $q = 0$ and upper limit $q = 27$ are also shown. All the quantities are dimensionless.

null geodesics, for *all* values of the observational angle. These sets of points are therefore curves of the (α, β) plane for different spins.

In details, the coordinate β is independent from the rotation orientation (sign of ℓ) and is upper bounded by the value $\beta^2 < 27$.

Let us concentrate on the **BH** counter-rotating (with $\ell = -\ell_H^-$) and the co-rotating ($\ell = \ell_H^-$) inner horizons replicas on the shadow profile shown in Figs (6) for different spins $a \in [0, 1]$ (solid curves) and angles $\sigma \in [0, 1]$. The black solid curve (outer curve in the left panel and inner curve in the center panel) represents the situation for the extreme Kerr **BH** ($a = 1$), and the blue solid curve (outer curve in the center panel and inner curve in the left panel) is for $a = 0.1$. (In other words, each solid curve represents the set of replicas on the shadows profiles for a fixed spin a . Each point of the solid curve is a replica for a *fixed* $\sigma \in [0, 1]$.) On the other hand, each dotted curve is the set of replicas for a *fixed* parameter σ . Each point of a dotted curve is for a specific **BH** spin. Black dotted curves correspond to $\sigma = 1$, blue dotted curves correspond to $\sigma \approx 0$. (In same cases, for graphical reasons, dotted curves have been extended beyond the intersections with the solid curves). On the left panel, $\sigma \approx 0$ is the inner limiting closed surface for the replicas in the shadow profile, while the equatorial plane, $\sigma = 1$, is the open limiting outer curve. On the center panel, the outer closed limiting dashed blue curve corresponds to $\sigma \approx 0$. For the co-rotating inner horizons replicas, the inner solid curve corresponds to the extreme **BH** spacetime ($a = 1$). The curves corresponding to replicas move outwardly (in the plane (α, β)) decreasing the value of the spin. Viceversa, in the counter-rotating case (counter-rotating inner horizons replicas), the extreme Kerr **BH** corresponds to the outermost curve of the plane, and the curves move inwardly with decreasing spin values. In all cases, β is upper bounded by the value $\beta = 3\sqrt{3}$. For $\ell = -\ell_H^+$, the value of β increases with the spin and with σ . There are no solutions for slowly spinning **BHs** and close to the **BH** poles. For $\ell = -\ell_H^-$, in general, β decreases with the **BH** spin and increases with σ . For $\ell = \ell_H^-$ (co-rotating inner horizon replicas) the results are similar to the case $\ell = -\ell_H^-$ (β is even in ℓ).

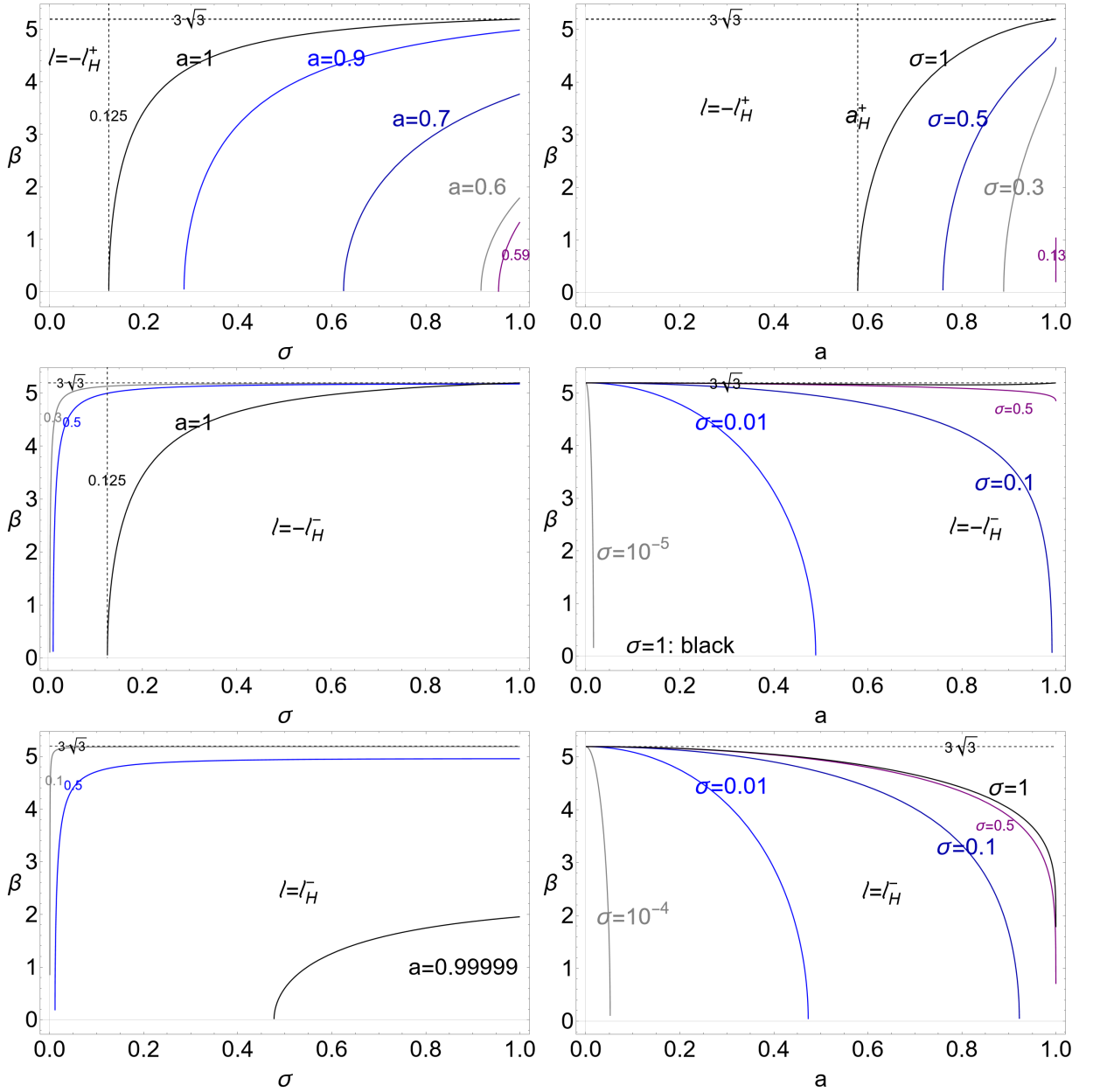


FIG. 5. The celestial coordinate β , solution of the set (\mathfrak{R}) of Eq. (10) with the constraint $\ell = -\ell_H^+$ (upper panels), $\ell = -\ell_H^-$ (center panels) and $\ell = \ell_H^-$ (bottom panels) (ℓ_H^\pm is the angular momentum of the outer and inner horizon respectively) as a function of the angular coordinate $\sigma \equiv \sin^2 \theta \in [0, 1]$ for different values of the spin a (left panels), and in terms of the spin a for different values of σ (right panels). The dotted lines are the limiting values of σ , β , and a . All the quantities are dimensionless.

V. DISCUSSION AND CONCLUDING REMARKS

This work explored the connection between **BH** shadow profile and horizons replicas, analysing the solutions of the equations (\mathfrak{R}) of Eq. (10) for the **BH** shadow profile, assuming constant ℓ coincident in magnitude with the angular momentum of the **BH** horizon $\ell_H^\pm(a)$ (horizons replicas). These special solutions of (\mathfrak{R}) are points and regions on the **BH** shadow luminous profiles, here highlighted and studied at different observational angles and for all values of the **BH** spin parameter. Conditions under which horizon replicas are imprinted in the **BH** shadows have been examined.

Replicas appear on particular regions of the orbital boundary defining the **BH** shadow. In this analysis, the β function is the significant celestial coordinate in the determination of the shadows topology and shape. The results are discussed in Sec. (IV) and in particular for the (α, β) coordinates in Sec. (IV B).

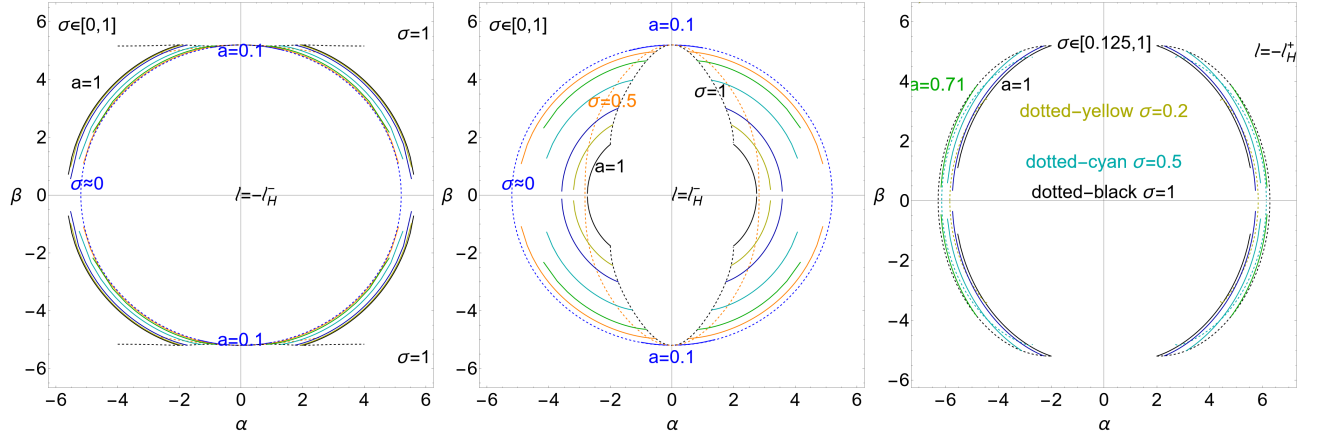


FIG. 6. Solutions of the set (\mathfrak{R}) of Eq. (10) (celestial coordinate β as function of α) with the constraint $\ell = -\ell_H^-$ (counter-rotating inner horizons replicas—left panel), for $\ell = \ell_H^-$ (co-rotating inner horizons replicas—center panel) and for $\ell = -\ell_H^+$ (counter-rotating outer horizons replicas—right panel) for different **BH** dimensionless spin $a \in [0, 1]$ (solid curves) and angles $\sigma \equiv \sin^2 \theta \in [0, 1]$. The quantities ℓ_H^\pm are the outer and inner horizons angular momenta, respectively. The black solid curve is $a = 1$ (outer curve in the left panel and inner curve in the center panel), the orange solid curve is $a = 0.5$, and the blue solid curve is for $a = 0.1$ (outer curve in the right panel and inner curve in the center panel). Each solid curve is the set of replicas on the **BHs** shadows profiles at fixed **BH** spin a . Each point of a solid curve is a replica for a fixed plane $\sigma \in [0, 1]$. Each dotted curve is the set of replicas on the **BHs** shadows profiles for a fixed plane σ . Each point on a dotted curve is for a specific **BH** spin. Hence, the crossing of the dotted and solid lines, fixes σ and the spin a . For the co-rotating inner horizons replicas (right panel), the inner solid curve corresponds to the extreme **BH** spacetime ($a = 1$). The replicas moves outwardly (in the plane (α, β)) decreasing the **BH** spin. Viceversa, in the counter-rotating case (counter-rotating inner horizons replicas—left panel) the extreme Kerr **BH** corresponds to the outermost curve of the plane, and the curves move inwardly decreasing the **BH** spin. Black dotted curves correspond to $\sigma = 1$, blue dotted curves correspond to $\sigma \approx 0$. (In same cases, for graphical reasons, dotted curves have been extended beyond the intersections with the solid curves for fixed $a \in [0, 1]$). On the left panel, $\sigma = 0$ is the inner limiting closed surface for the replicas in the shadow profile, while the equatorial plane, $\sigma = 1$, is the open limiting outer curve (confinement on the equatorial plane). On the center panel the outer closed limiting dashed blue curve corresponds to $\sigma \approx 0$. Right panel: the inner black solid curve is for $a = 1$ and the green outer curve for $a = 0.71$. All quantities are dimensionless.

More in details:

From a methodological view–point, we solved Eqs. (10) (referred as set (\mathfrak{R})) fixing $\ell = \pm\ell_H^\pm$. In general, for fixed a and σ , the **BH** shadow profile is found in terms of solutions of the set (\mathfrak{R}) for *all* values of ℓ and r . Solutions are, therefore, closed curves $\beta(\alpha)$ (black curves of Figs (7)). Solving (\mathfrak{R}) with constraints on ℓ , and *fixing* (a, σ) , we obtain a set of points (α, β) on the shadow profile corresponding to the fixed **BH** spin a and observational angle σ (vertical lines in Figs (7)). On the other hand, solving (\mathfrak{R}) with constraints on ℓ , at *fixed* a and for *all* values of the observational angle σ , provides a set of points on the shadow profile representing the superposition of the points on the shadow boundary relative to the constrained null geodesics, for *all* values of the observational angle. These sets of points are, therefore, curves of the (α, β) plane, and they are shown, for example in Figs (6) for different spins. In these panels, each curve corresponds to a *fixed* spin and a specific constraint, and each point of each curve is for a different σ . In this way, we obtained, for *all* **BH** spins, a map of the constrained regions on the shadow profiles, for *all* the observational angles. We also related, for each constraint, the quantities $(a, \sigma, r, \ell, q, \beta)$ — Fig. (3,4,5). The quantities (a, r) in the constrained solutions of (\mathfrak{R}) are related as shown in Figs (2). The relations (σ, r) and (σ, a) from the solutions (\mathfrak{R}) with the constraints are in Figs (3). This analysis set the range of values for the observational angle σ and for range of spin a , where replicas appear on the **BH** shadow luminous boundary. The quantities (q, a) and (q, r) , constrained solutions of the set (\mathfrak{R}) , are in Figs (4).

The results of this analysis, illustrated in details in Sec. (IV A), show that, in general, the radius r is bounded in a small range of values (around $r = 3$ for any spin and angle θ) and the angle σ is, in general, bottom bounded according to Figs (2,3,4). The results are then confirmed from the analysis in Figs (5,6).

–In Figs (5), celestial coordinate β (solution of the set (\mathfrak{R}) with $\ell = -\ell_H^+$ and $\ell = \pm\ell_H^-$) is shown as a function of the angular coordinate σ for different spin a signed on the curves (left panels), and in terms of the spin a for different values of σ signed on the curves (right panels).

–In Figs (6), the coordinates β and α , solutions of (\mathfrak{R}) with the constraint $\ell = -\ell_H^-$ (left panel), for $\ell = \ell_H^-$ (center panel) and for $\ell = -\ell_H^+$ (right panel), are shown for different **BH** spins $a \in [0, 1]$ (solid curves) and angles σ . Each

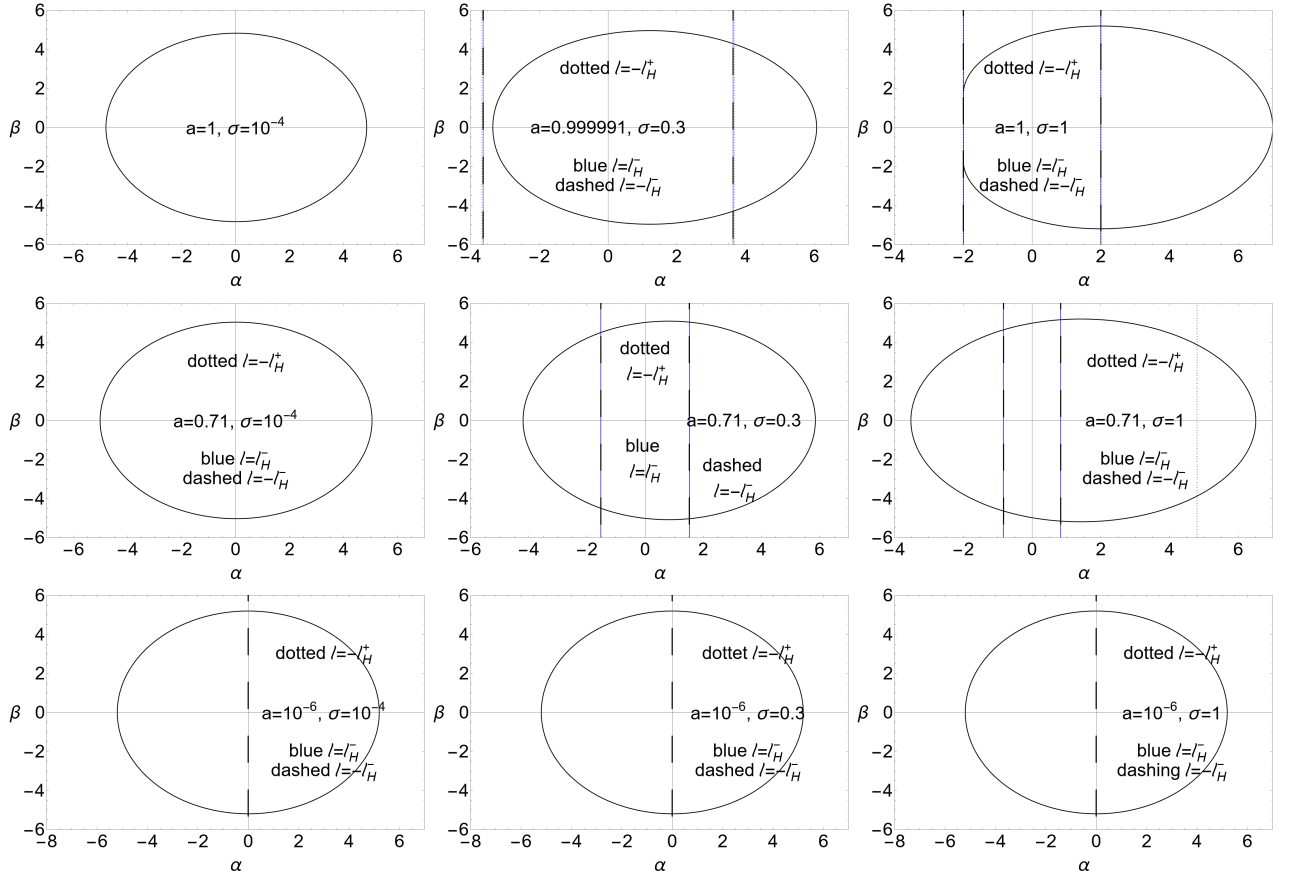


FIG. 7. **BH** shadow profiles (closed black curves) solutions of the set (\mathfrak{R}) of Eq. (10) (celestial coordinate β versus α), for *all* values of the impact parameter ℓ , and for different dimensionless spins $a \in [0, 1]$ and angular coordinate $\sigma \equiv \sin^2 \theta \in [0, 1]$, denoted on the panels. Vertical lines on the panels are solutions of the set (\mathfrak{R}) (celestial coordinate β versus α), for $\ell = \pm \ell_H^\pm$ (ℓ_H^\pm are the outer and inner horizons angular momenta) and for fixed a and σ . The upper row is for $a \approx 1$, middle row for $a = 0.71$, bottom row for $a \approx 0$, left column for $\sigma \approx 0$, center column for $\sigma = 0.3$, and right column for $\sigma = 1$. (All quantities are dimensionless).

point (α, β) of a curve provides the corresponding solutions on the **BH** shadow profile. The crossing of the dotted and solid lines fixes σ and the spin a . Each solid curve corresponds to the set of replicas on the **BHs** shadows profiles at *fixed* **BH** spin a and a specific constraint, and each point of each curve is a replica for a fixed angle σ , where each dotted curve is the set of replicas on the **BHs** shadows profiles for a fixed plane σ . (Each point on a dotted curve is for a specific **BH** spin.). Remarkably, the radial distance from the central attractor is $r < 3.8$, considering co-rotating and counter-rotating orbits from any planes and for any spin, where the celestial coordinate is upper bounded by the value $\beta < 3\sqrt{3}$. There are no solutions for the condition $\ell = \ell_H^+$ (co-rotating outer horizon replicas). It is clear that the counter-rotating replicas of the outer horizons can be observed far from the rotational axis for fast spinning black holes, i.e., for $a \gtrsim 0.59$ with $\sigma \gtrsim 0.125$.

—In Figs (7), **BH** shadow profiles (solutions of the set (\mathfrak{R}) of Eq. (10) for *all* values ℓ), are shown for different spins $a \in [0, 1]$ and σ (closed black curves). Vertical lines point to the solutions corresponding to null geodesics of the set (\mathfrak{R}) with the constraints $\ell = \pm \ell_H^\pm$.

The constraints we set are therefore related to particular regions of the orbital boundary (luminous edge) defining the **BH** shadow. The imprints of replicas (coordinates (α, β) solutions of constrained (\mathfrak{R})) on the shadow boundary of the central Kerr **BH** map the luminous edge at different observational angles, and for all **BH** spins. Distinguishing in particular co-rotating and counter-rotating photons, for fixed plane σ and spin a (as shown in Figs (7)) and for *all* planes σ and spin a .

The existence and location of replicas on the shadow profiles vary according to the value of the spin; for some spins there are no replicas. This fact has remarkably consequences from an observational viewpoint as it constitutes a valid discriminant for the evaluation of the **BH** spin. The new observables are related to particular photon orbits, carrying information in their impact parameter about the angular momentum of the rotating **BH**, to potentially accompany

other existing methods and techniques to detect and measure the spins of an accreiting **BH**. These methods consist for example of **X**-ray reflection spectroscopy (see [62]), or gravitational waves detection of **LIGO-Virgo-KAGRA (LVK) Collaboration**¹⁰ [63]. (We should also stress that **BH** shadows can depend on properties of the region of the light distribution and its source for example accretion disks, where photons could interact with the accreiting plasma. Our analysis can be adaptable to and complement the constraints imposed by the specific numerical or analytical model of accretion disks—see for example **EHT** Collaboration compared numerical torus models directly to observations in several comprehensive analysis [5, 14] see also [2, 4, 6, 8, 15, 47, 64–75].).

Analysis of the photons parameters ℓ could help understanding the **BH** energetic processes. (In particular the poles of a Kerr **BH**. The quantity ℓ , the photons impact parameter (specific angular momentum) adopted here to discern the photons, plays also a significant role in **BHs** accretion physics, limiting the **BH** energy extraction with the limiting quantity ℓ evaluated on the outer horizon.). An interesting aspect to explore further is the relevance of the horizons replicas, observable in **BH** shadows, for the **BH** magnetosphere constraints. Light surfaces (related to the horizons replicas) are widely adopted in the analysis of the **BH** magnetosphere—see for example [76, 77]—, constraining the electromagnetic fields, which link, for example, the disk to the central **BH** attractor¹¹. The consequences of the existence of horizons replicas on the **BH** magnetosphere will be considered in future analysis.

However results found in this analysis could constitute a new template of observations (and a way to identify the central attractor constraining the **BH** dimensionless spin) in future observational enhancements.

More specifically, we should consider that the current **EHT** images consist of unresolved rings composed by sets of (infinite) narrow self-similar sub-rings (photon orbits), which are usually indexed by the photon orbits numbers $n \in \mathbb{N}$ around the **BH** (for photons circling the attractor $n/2$ times before reaching the observer), approaching and converging, asymptotically, the **BH** shadow boundary¹². The critical curve defines the region of light rays captured by the photon shell and (unstably) orbiting the **BH**, falling into the **BH**, or escaping to infinity. The **BH** shadow itself is the interior of the critical curve. The number of oscillations of the light rays, very near the critical curve diverges logarithmically as the coordinate approaches a point on the critical curve. Each point of the curve, parametrized with the (α, β) coordinates, is associated with a null geodesic labeled by the two conserved quantities (ℓ, q) which, as done in our analysis, in turn can be retraced to infer information on the **BH** properties.

On the other hand, resolved **EHT** images in the sub-rings, could provide a method to determine the **BH** parameters by evaluating for example the sub-rings morphological characteristics as size, shape, or thickness¹³ that use the ring shape, sub-rings and a variety of models considered for the source.

The main morphological photon ring characteristics, however, are below the current **EHT** imaging resolution. The present (as for **M87***) array coverage does not allow the extraction of dim features below $\approx 10\%$ of the peak

¹⁰ <https://www.ligo.org/index.php>; <https://www.virgo-gw.eu>; <https://gwcenter.icrr.u-tokyo.ac.jp/en/>

¹¹ For an electromagnetic field in Kerr spacetime with $\omega < \omega_H^+$, light surfaces (**LSs**) are surfaces where the magnetic field lines (co)-rotate (with ω) at the speed of light. ($\omega < \omega_H^+$ is the outer horizon tangency condition in the bundle approach (see Sec. (A 1)), and it constrains the energy extraction from the **BH**. In the bundles framework, however, we consider also the counter-rotating condition for fixed $\omega < 0$). In the Kerr **BH** spacetime, there are two **LSs**. The inner one is inside the ergoregion and one is outside the ergoregion [78–83], corresponding to the Pulsar light cylinder asymptotically. The **BH** magnetosphere, rigidly rotating with angular velocity ω , is divided into sub-luminal and super-luminal rotation regions, depending on $\mathcal{L}_{\mathcal{N}} \equiv \mathcal{L} \cdot \mathcal{L}$ sign ($\mathcal{L} \equiv \xi_{(t)} + \omega \xi_{(\phi)}$). The separating surfaces, solutions of $\mathcal{L}_{\mathcal{N}} = 0$, are **LSs** [84–86]. Thus, outside of the outer **LS**, magnetic field lines would rotate faster than the speed of light (respect to ZAMOs). Inside the inner **LS**, magnetic field lines would (counter)rotate super-luminally with respect to the ZAMO [78, 79, 84, 87–94] In the Grad-Shafranov (GS) equation (from the poloidal component of the force-balance equation) for the Kerr magnetosphere, ω is the velocity of the magnetic field lines. In the **BH** magnetospheres, in the force-free limit, the **LSs** correspond to two singular surfaces (together with the event horizon, which coincides with the singular surfaces of the Alfvén waves—the relativistic generalization of the Alfvén points in force-free conditions). On **LSs**, regularity conditions can be set to determine the poloidal current as a function of the poloidal magnetic flux. The event-horizon regularity condition (Znajek horizon boundary condition) can be used to determine the poloidal flux distribution on the horizon. The GS equation is a second-order differential equation for the magnetic flux with two eigenfunctions I and ω to be determined, for example, by requiring that the magnetic field lines smoothly cross the **LSs**, where the GS is a first-order differential equation. Therefore, the **LSs** are found by imposing that the second-order derivatives of the GS equation vanish there. The solution depends on the distributions of the magnetic field lines angular velocity $\omega(\psi)$ and the poloidal electric current $I(\psi)$, which can be determined self-consistently by assuming that the magnetic field lines cross the inner and outer **LSs**. Clearly, the event horizon corresponds to the solution of the singularity condition for $\omega = \omega_H^+$, explained in the bundles frame.

¹² **EHT** observations of the horizon scale emission of **M87*** could support the presence of a "narrow ring-like" feature [43]. On the other hand, evidence for the presence of a lensed photon ring in the 2017 **M87*** observations was discussed in [41]. It has been argued that the photon ring (simultaneously with the "inner shadow") could be visible in sub-millimeter images of **M87*** from **VLBI**, and the photon ring morphology and inner shadow can be used to provide a **BH** mass and spin estimation—[95]. The structure of emission inside the critical curve has been considered for equatorial-disk emission models—see also [49, 95]. A discussion on the possibility that multiple measurements of the photon rings of **M87***, could resolve the ring size and guess the emission region, is presented in [44]. There, it is also claimed that mass and spin may be guessed by the $n = 2$ photon ring.

¹³ For example, the measurement of the **M87 BH** spin from its observed twisted light was considered in [20] (by the characterization of the electromagnetic waves vorticity from the **BH** surroundings).

brightness, i.e., it is estimated that the lensed images account for $\approx 10\%$ of the flux (**GRMHD** simulations suggest that the photon ring should provide only $\approx 10\%$ of the total image flux density, hence precluding to the current observations the determination of photon ring and the resolution of its substructure)¹⁴.

However, we should consider that the inference of the underlying image of the **EHT** observation features is probabilistic, using a variety of possible analytical models and image reconstruction based on geometric modelling. Imaging algorithms provide a best fitting image—[9]. The characteristics considered in this analysis should be processed with observations constrained by the current resolution limits of **EHT** and also by the different data analysis implemented. In the more straightforward scenario, this would require distinguishing lensed sub-rings within the observed image with limited-resolution observations where, for example, the systematic uncertainties may be reduced using an enhanced ground or space-based array. Furthermore, the restriction of the dynamic range and visibility coverage could be addressed by appropriate modeling and imaging able to disentangle the ring-like emission structure, for example, focusing on multiple image reconstruction algorithms—[46].

Hence, until such limitations will be reduced any efforts to use more detailed edge properties will be considered for future implementation or enhanced technics (possible sub-rings resolution methods in **EHT** extensions are discussed in [47], arguing on the possibility of measurements photon sub-ring from an high-frequency ground array or low Earth orbits, and from Moon station.) The results we prove here may be used in the frame of future observations by a next-generation **EHT**, with proposed future Earth-based arrays and possibility of space-based stations, with their associated long baselines which could resolve first orders photon rings. Indeed, in coming years more radio telescopes will be added to the **EHT** array, resulting in a larger and more sensitive array and increasing the dynamic range of the current **EHT** of several factors, higher-frequency observations will be possible, reaching higher signal-to-noise ratios and much better baseline coverage, obtaining an overall improved sensitivity.

ACKNOWLEDGEMENTS

The work of HQ was supported by UNAM PASPA-DGAPA.

Appendix A: Notes on metric bundles and characteristic frequencies

In this section we provide more details on the concepts of metric bundles and replicas used to constrain solutions of system (\mathfrak{A}). In Sec. (A 1) the concept of metric bundles and replicas is deepened. Relations between definition of photon circular orbits and replicas are discussed in Sec. (A 2). Sec. (A 2 a) clarifies the relation between concepts of photons spheres and replicas. In Sec. (A 2 b) we relate circular photons orbits and replicas.

1. Metric bundles and replicas

In this section we introduce the concept of metric Killing bundles (**MBs**) used to constrain solutions of system (\mathfrak{A}). **MBs**, extensively studied in [32–38], are defined as the collections of light-like circular orbits with the same constant orbital frequency ω , which is called *characteristic bundle frequency*. This frequency results to be also the frequency of a **BH** horizon of the corresponding collection.

Frequencies ω_H^\pm

We start by introducing the quantities ω_H^\mp (the inner and outer horizon frequencies respectively) from the definition of **BH** Killing horizons.

The event horizons of a spinning **BH** are Killing horizons with respect to the Killing field $\mathcal{L}_H^\pm = \xi_{(t)} + \omega_H^\pm \xi_{(\phi)}$.

¹⁴ The critical curve analysis from direct observation would imply the detection of lensed sub-rings, possible only with a very-high resolution baselines. It remains possible to eventually *infer* the features of the critical curve by implementing adapted method to the resolution of the sub-rings. A set of astrophysical models has been analysed and different resolution techniques have been implemented. Furthermore, the ring can exhibit additional substructure due to the presence of not uniform light source as for example an accretion disk. Indeed, it should also be considered that the analysis is complicated by the fact that, the size, shape, and depth of the observed brightness depression depend on the peculiarities of the emission process and emission region. (**GRMHD** simulations are primary tools to resolve the features of the **EHT** images, which are currently unable to structure the inner shadow due to lack of resolution and dynamic range, hopefully reachable in the next-generation **EHT**.) Therefore, the bundle of photon rings, substructuring the final image, encodes both the emission (governed by the orbiting matter and emission processes) and the spacetime properties (determined by the **BH** only).

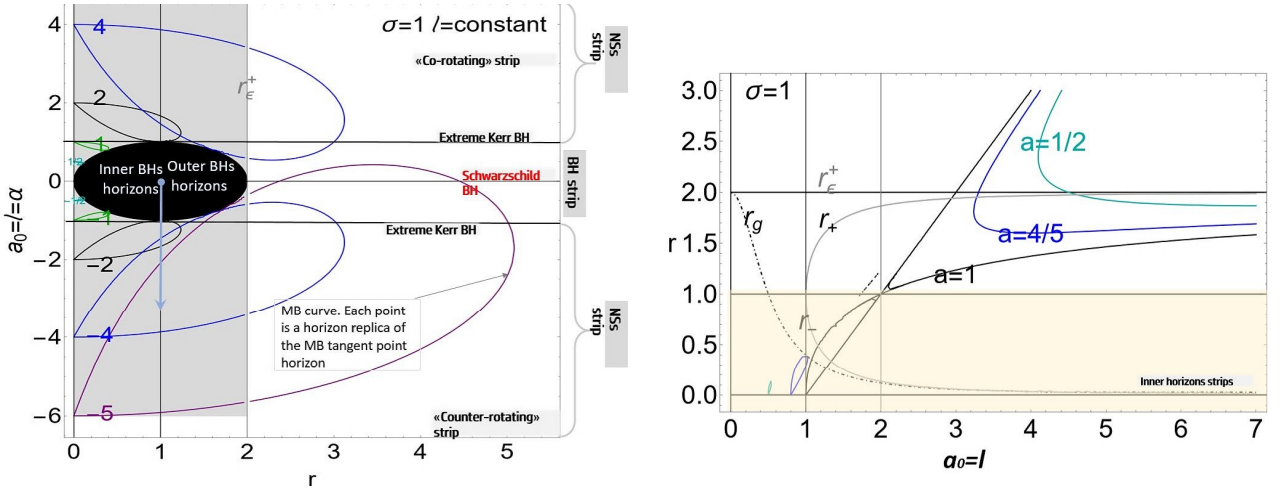


FIG. 8. Left panel: Extended plane $a - r$ on the equatorial plane ($\sigma = \sin^2\theta = 1$) of the Kerr geometry. Metric bundles (**MBs**) with characteristic frequency ω and angular momentum $\ell = 1/\omega = a_0 = \text{constant}$ are shown for different values of ℓ , which are denoted on each curve. The quantity a_0 represents the bundle origin spin at $r = 0$, which coincides with celestial coordinate α —Eq. (14). The **BH** region is shown in black and the outer and inner horizons a_{\pm} are depicted as functions of r . A horizontal line on the extended plane at $\sigma = 1$ represents a fixed spacetime $a = \text{constant}$. In particular, $a = 0$ corresponds to the Schwarzschild **BH** spacetime and $a = 1$ to the extreme Kerr **BH**. In the region $a^2 > 1$, there are the naked singularity (**NS**) strips. The angular momentum of the inner and outer horizons curve are shown explicitly. The momentum $\ell_H^{\pm} = 2$ corresponds to the extreme Kerr **BH**. On the equatorial plane, the point $r = 2$ is the outer ergosurface and the Schwarzschild **BH** horizon corresponds to $a = 0$. All quantities are dimensionless. Right panel: Light surfaces $r(\ell; a)$ are solutions of the condition $\mathcal{L}_{\mathcal{N}} = 0$ are shown as functions of the momentum ℓ for different **BH** spin values that are signed on the curve. Here, $\omega = 1/a_0$ corresponds to $r = 0$. r_g is the tangent curve of the metric bundles as function of ℓ . The radii r_{\pm} denote the outer and inner horizons; the radius r_e^+ is the outer ergoregion on the equatorial plane. All quantities are dimensionless.

Defining the more general Killing field $\mathcal{L}_{\omega} \equiv \xi_{(t)} + \omega \xi_{(\phi)}$, the quantity $\mathcal{L}_{\omega} \equiv \mathcal{L}_{\omega} \cdot \mathcal{L}_{\omega}$ becomes null for photon-like particles with rotational frequencies ω_{\pm} . We define also the *angular momentum* $\ell \equiv 1/\omega_{\pm}$.

Therefore, **MBs** correspond to the set of all solutions of the condition $\mathcal{L}_{\mathcal{N}} = 0$ for a fixed ω (ℓ).

MBs also constraint the *stationary observers* as their four-velocity u^{α} is a linear combination of the two Killing vectors $\xi_{(\phi)}$ and $\xi_{(t)}$; therefore, $u^{\alpha} = \gamma \mathcal{L}^{\alpha} = \gamma(\xi_{(t)}^{\alpha} + \omega \xi_{(\phi)}^{\alpha})$, where γ is a normalization factor and $d\phi/dt = u^{\phi}/u^t \equiv \omega$. The dimensionless quantity ω is the orbital frequency of the stationary observer bounded in the range $\omega \in]\omega_-, \omega_+[$. Hence the limiting frequencies ω_{\pm} are the photon orbital frequencies solutions of the condition $\mathcal{L}_{\mathcal{N}} = 0$. ω_{\pm} . On the other hands the solutions $r(\omega) : \mathcal{L}_{\mathcal{N}} = 0$ for a fixed a define the light surfaces. Metric bundles and light surfaces are represented in Figs (8).

The light-like orbital frequencies ω_{\pm} and the horizons frequencies ω_H^{\pm} satisfy the following relations

$$\omega_H^{\pm} \equiv \frac{r_{\mp}}{2a}, \quad \text{with} \quad \lim_{r \rightarrow r_{\pm}} \omega_{\pm} = \omega_H^{\pm}, \quad \lim_{r \rightarrow 0} \omega_{\pm} = \pm \frac{1}{a\sqrt{\omega}}, \quad \lim_{r \rightarrow \infty} \omega_{\pm} = 0, \quad (\text{A1})$$

where $\omega_H^- \in]+\infty, 1/2]$ and $\omega_H^+ \in [1/2, 0]$. The frequency $\omega_H^{\pm} = 1/2$ corresponds to the extreme Kerr **BH**.

The extended plane

A **MB** can be represented as a curve in the *extended plane*, which is defined as a plane $\mathcal{P} - r$ with \mathcal{P} being a parameter or function that characterizes the Kerr spacetime. In particular, we will use the extended planes $a - r$ and $\mathcal{A} - r$, where $\mathcal{A} \equiv a\sqrt{\sigma}$ and r is the radial BL coordinate.

In the extended plane $a - r$, all the curves representing **MBs** (*bundle curves*) are tangent to the horizons curve (the curve $a_{\pm} \equiv \sqrt{r(2-r)}$, which represent the Killing horizons of all Kerr **BHs**)—see Figs (8)¹⁵. It follows that the horizons in the extended plane emerge as the envelope surface of all the metric bundles.

¹⁵ This tangency condition implies that each bundle characteristic frequency ω coincides with the frequency ω_H^{\pm} of a Killing horizon of the **BH** tangent to the curve. All the metric bundles curves are always tangent to the horizon curve in the extended plane—Figs.(11)—consequently there is always a **BH** horizon (a, r_{\pm}) which is part of the bundle, therefore the bundle characteristic frequencies are always a **BH** horizon frequency (the frequency of the **BH** horizon correspondent to the point tangent to the bundle curve in the extended

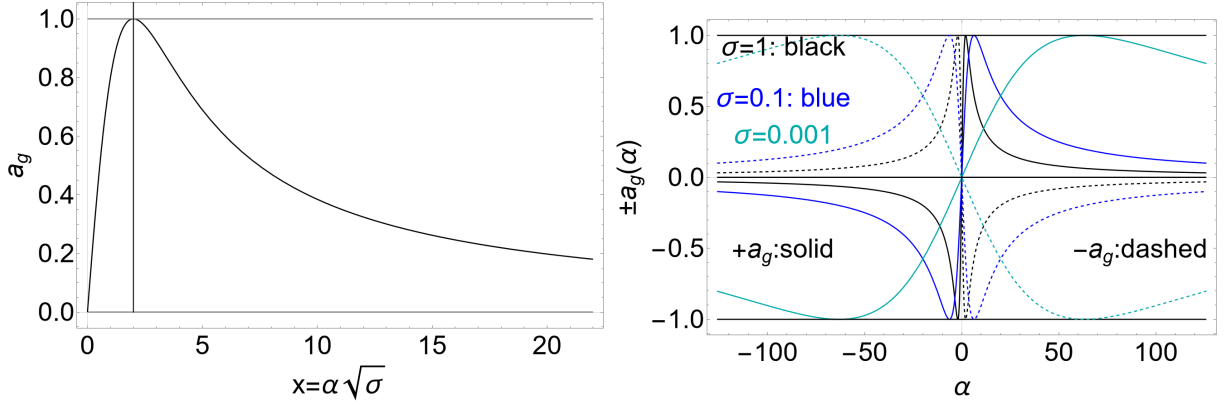


FIG. 9. Left panel: Tangent spin a_g (tangent spin of the metric bundle curve in the extended plane) as a function of $x = \alpha\sqrt{\sigma}$, equivalent to $a_g(\alpha)$ for $\sigma = 1$, where $\alpha = -\ell/\sin\theta$ is the celestial coordinate, which coincides with the bundle origin. ℓ is the photon specific angular momentum and $\sigma \equiv \sin^2\theta \in [0, 1]$. Right panel: The functions $\pm a_g(\alpha)$ for different planes σ . All quantities are dimensionless.

The concept of metric bundles and some of their main features are illustrated in Fig. (8), in the extended plane $a - r$ of the equatorial plane ($\sigma = 1$) of the Kerr geometry. Note that the extended plane can be extended to values $a < 0$ to consider the counter-rotating photons.

The left panel of Fig. (8) shows metric bundles at $\sigma = 1$ for different characteristic frequencies $\omega = 1/a_0 = \text{constant}$, where a_0 is the *bundle origin spin* (or bundle origin), defined in Eqs. (A1). The right panel of Fig. (8) shows the light surfaces as functions of the bundle origin on the equatorial plane.

The characteristic bundle angular momentum is $\ell \equiv 1/\omega = a_0$. For $\sigma \in]0, 1[$ the bundle origin spin is $\mathcal{A}_0 \equiv 1/\omega\sqrt{\sigma}$, corresponding to the solution $a : \mathcal{L}_{\mathcal{N}} = 0$ for $r = 0$.

On the extended plane $a - r$, the point (a_g, r_g) is the tangent point of the bundle to the horizons curves. Therefore, the bundle origin spin \mathcal{A}_0 bundle tangent radius $r_g(\omega)$ as function of the **MB** frequency and bundle tangent spin $a_g(a_0)$ as function of the origin spin a_0 are

$$\mathcal{A}_0(\omega, \sigma) \equiv \pm \frac{\csc(\theta)}{\omega} = \pm \frac{1}{\omega\sqrt{\sigma}} = \frac{\ell}{\sqrt{\sigma}} = -\alpha, \quad r_g(\omega) = \frac{2}{4\omega^2 + 1}, \quad a_g(a_0) \equiv \frac{4a_0\sqrt{\sigma}}{a_0^2\sigma + 4}. \quad (\text{A2})$$

there is $r_g \in [0, 1]$ for $r_g = r_-$ and $r_g \in [1, 2]$ for $r_g = r_+$ —see for example [32]. Note that α in Eq. (14) coincides with the bundles origin spin $\alpha = -\mathcal{A}_0 \equiv -1/(\omega\sqrt{\sigma}) \equiv -\ell/\sqrt{\sigma}$ for co-rotating ($\ell > 0$) and counter-rotating photons ($\ell < 0$). As $\alpha = a_0 \in [-\infty, +\infty]$, then $a_g(a_0) \in [0, 1]$ is a way to express the horizon curves in the extended plane as function of the bundles origin (here restricted to the positive plane $a_g > 0$). In this case, as $\alpha = a_0 = 1/\omega = \ell \in [-\infty, +\infty]$, $a_g(\alpha) \in [0, 1]$ is a way to express the horizons curves in the extended plane as function of the celestial coordinate α —see Figs (9). The function $a_g(a_0)$ establishes a relation between the bundle tangent spin, a **BH** horizon, and a bundle origin spin. The tangent spin can be associated to two tangent radii, corresponding to an inner or an outer horizon (depending on the values of a_0). The function $a_g(\alpha)$ associates the spin a_g to the celestial coordinate α for a fixed plane σ and can be parameterized for $x = \alpha\sqrt{\sigma} = 1/\omega = \ell$. Therefore, for a fixed $a = a_g$ there are two couples of (α, σ) in the **MBs** framework, corresponding to the inner and outer horizon frequencies, respectively, see also Figs (9).

For $\ell = \alpha = 2$ there is one couple, which corresponds to the extreme Kerr **BH** with $a_g = 1$. Obviously, the product $\alpha\sqrt{\omega}$ is, in general, different for the two couples because they correspond to the angular momentum of the inner and outer horizons. The maximum point of $a_g(\alpha)$ for x or α (σ) is for $a_g = 1$ and $\alpha = 2/\sqrt{\sigma}$.

From the definition of α we find the spin function

$$a = a_g(\alpha) = \frac{4\alpha\sqrt{\sigma}}{\alpha^2\sigma + 4} \in [0, 1], \quad (\text{A3})$$

plane). Hence one could say that all points r of the bundle curve (also in the **NSs** spacetimes) are replicas of the **BH** horizon of the tangent point. In this work we constrain the co-rotating and counter-rotating replicas in the same spacetime of the tangent point (horizontal lines of Figs (11)).

(which coincides with *bundle tangent spin* of Eq. (A2) expressing the **BH** horizons curve). For $\alpha = 0$ and $\alpha = \infty$ there is $a_g = 0$ —Figs (9)—left panel.

In Sec. (A2), we discuss in details the relation between bundles null-orbits and photon circular orbits on the equatorial plane.

Horizons replicas

In our analysis we study solutions of the set (\mathfrak{R}) of Eq. (10) with the constraint $\ell = \pm\ell_H^\pm$ therefore on the inner and outer horizons replicas, on the same **BH** spacetime of the bundle curve tangent point to the horizons, which are special points on the **MBs** curves (determined by the horizontal lines in the extended plane).

Horizon replicas are special light-like circular orbits of a Kerr spacetime with frequency equal to the **BH** (inner or outer) horizon frequency, which coincides with the bundle characteristic frequency in the corresponding point on the extended plane¹⁶. According to the definition of metric bundles, there are clearly replicas in different geometries. For instance, to the points (\mathcal{P}, r) and $(\bar{\mathcal{P}}, \bar{r})$ on the bundle curve of the extended plane, there can correspond the same light-like orbital frequency¹⁷. Metric bundles have been defined by using the condition that the quantity $\omega = u^\phi/u^t$ is a constant on photon circular orbits. An analogue definition can be set in terms of ℓ , which is a constant of the geodesic motion that is related by $\ell = 1/\omega\sqrt{\sigma}$ (with an analogue definition for the counter-rotating motion) with the characteristic frequency ω of a metric bundle. Then replica of the outer and inner horizon are

$$\omega_H^\pm : r = \frac{a^2 \left(\sqrt{10r_\mp - a^2} - r_\mp \right)}{2(2r_\mp - a^2)} \quad (\text{A4})$$

respectively where $\omega_H^\pm = \omega(\ell_H^\pm, r)$, are the outer and inner horizon frequencies— see Figs (10). We restricted our analysis to the co-rotating case. Furthermore, in certain cases, for example in Kerr naked singularities, the condition $\omega < 0$ does not always correspond to $\ell < 0$.

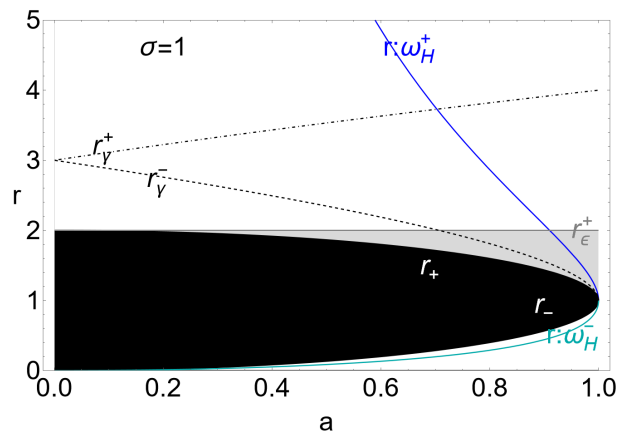


FIG. 10. Replicas of the inner and outer horizons on the equatorial plane $\sigma \equiv \sin^2 \theta = 1$. The radii r_\pm are the outer and inner Kerr **BH** horizons, respectively. $r_\epsilon^+ = 2$ is the radius of the outer ergoregion on the equatorial plane, a is the **BH** dimensionless spin, ω_H^\pm are the outer and inner **BH** horizon frequencies, respectively. All quantities are dimensionless. Black regions denote **BH** region. On the equatorial plane, the inner horizon frequencies are confined and the photons cannot reach the observer. Radii r_γ^\pm are the counter-rotating and co-rotating photon circular orbits (marginally circular orbit) on the equatorial plane and boundary of the Kerr **BH** spacetime photon sphere.

¹⁶ Viceversa, the **MBs** *horizon confinement* is a concept interpreted as due to the presence of a “local causal ball” in the extended plane, which is a region, where the **MBs** are entirely confined, i.e., there are no horizon replicas in any other region of the extended plane outside the causal ball. In the Kerr extended plane, a causal ball is the region upper bounded by a portion of the inner horizon, which means that the horizon frequencies defined for these points of the inner horizons cannot be measured (locally) outside this region.

¹⁷ Replicas can, therefore, be used also to relate *different* spacetimes. This possibility could be useful in some scenarios featuring transitions from **BH** to **BH**, following the changing of some parameters such as charge, mass, and momentum as regulated by the laws of **BH** thermodynamics, or to explore some theoretical concepts concerning relations between black holes and naked singularities. These aspects have been explored, for example, in [33–35]. However, in this work, we do not consider this situation, but we fix the **BH** spin (for any value $a \in [0, 1]$) and analyze its horizon replicas. We do not compare orbits and horizons of different Kerr solutions in the parameter space but focus instead on the possibility of detecting the **BH** horizons replicas imprint on its shadows profiles, fixing therefore the **BH** spacetime and considering the existence of replicas in the *same* spacetime.

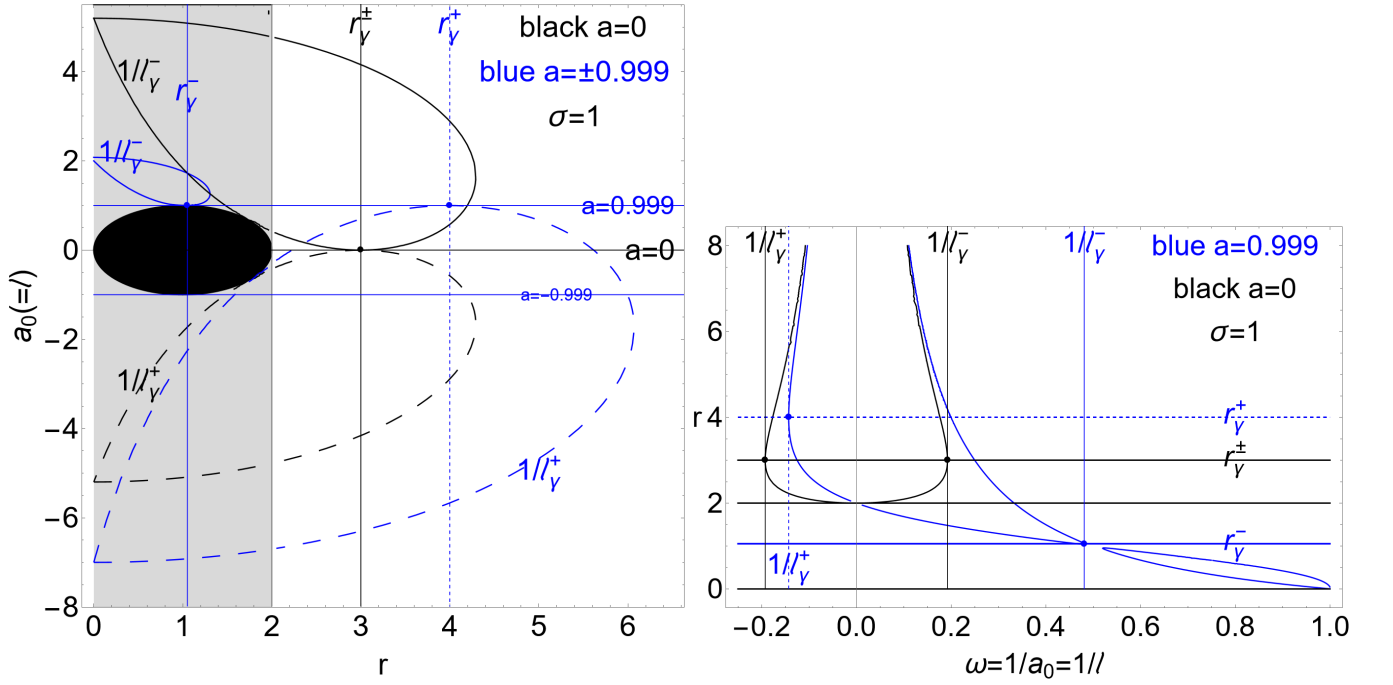


FIG. 11. Analysis of the equatorial co-rotating (solid curves) and counter-rotating (dashed curves) photon circular orbits in the extended plane (left panel) and light surfaces (right panel) frame. See the discussion in Sec. (III C). The case $a = 0$, corresponding to the Schwarzschild **BH** spacetime (black curves), and the Kerr **BH** $a = \pm 0.999$ (blue curves) are plotted. All quantities are dimensionless. The extended plane $a - r$ (left panel) and light surfaces (right panel) $r(\omega)$, as functions of the bundles characteristic frequencies ω (limiting photon orbital circular frequencies of the stationary observers), are represented on the equatorial plane ($\sigma = \sin^2 \theta = 1$) of the Kerr geometry. On the left panel, the black central region is the **BH** region bounded by the horizons curves. The gray region is the ergoregion $r \in]0, r_{\epsilon}^+]$, where $r_{\epsilon}^+ = 2$ is the outer ergosurface on the equatorial plane. The metric bundles (**MBs**) with characteristic frequency ω and angular momentum $\ell = 1/\omega = a_0 = \text{constant}$ are shown for different values of ℓ , signed on each curve. The quantity a_0 represents the bundle origin spin at $r = 0$ (which coincides with the celestial coordinate α). The radii r_{γ}^{\pm} are the counter-rotating and co-rotating photon circular orbits (marginally circular orbits), respectively. The quantities ℓ_{γ}^{\pm} are the orbital specific angular momentum of counter-rotating ($\ell a < 0$, $\omega < 0$) and co-rotating ($\ell a > 0$, $\omega > 0$) photon circular orbits, respectively, where $\ell \equiv \mathcal{L}/\mathcal{E}$ and the constants of motion (\mathcal{L}, \mathcal{E}) are the angular momentum and energy (as measured at infinity), respectively. The light surfaces $r(\ell; a)$ are solutions of the condition $\mathcal{L}_{\mathcal{N}} = 0$ (on $\sigma = 1$) and are shown as functions of the momentum ℓ for different **BH** spin values. On the extended plane at $\sigma = 1$, a horizontal line represents a fixed spacetime $a = \text{constant}$. The points represent the equatorial photons circular orbits (marginally circular orbit) of the spacetime.

2. On photons orbits and replicas

In this section we focus on the relation between replicas, metric bundles, photons circular orbits, photons sphere (or photon shell) –see also [47, 96]. In Sec. (A 2 a) we discuss the relation between concepts of photons spheres and replicas. In Sec. (A 2 b) we relate circular photons orbits and replicas.

Only some replicas are orbits of the photon sphere, and only some photon circular orbits are replicas, on the other hand only some replicas are solutions of the system (\mathfrak{R}) . These particular solutions of (\mathfrak{R}) , providing the shadow boundary (for example black curves of Figs (7), are found by solving (\mathfrak{R}) with the constraints $\ell = \pm \ell_H^{\pm}(a)$, and emerge as points on the shadow profile (for example vertical lines¹⁸ of Figs (7)).

¹⁸ Considering for example the case for $a = 0.71$ and $\sigma = 0.3$ ($\theta = 0.5796$), represented in Figs (7), for $\ell_H^- = 0.833$ (co-rotating inner horizon replica), there is $\{\alpha, \beta\} = \{-1.52, 4.5\}$ and $\{r, q\} = \{2.59, 21.5\}$, and for $\ell_H^+ = -0.833$ (counter-rotating inner horizon replica) there is $\{\alpha, \beta\} = \{1.521, 5.036\}$ and $\{r, q\} = \{2.89988, 26.6343\}$.

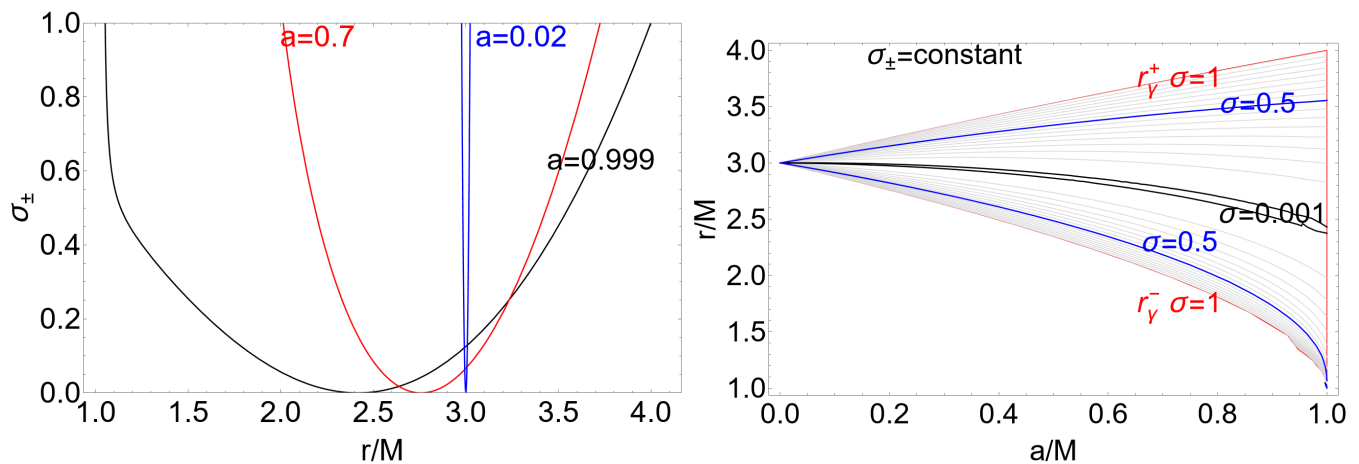


FIG. 12. Left panel: planes σ_{\pm} of Eq. (A5), limiting the Kerr spacetime photon sphere (where $\sigma \equiv \sin^2 \theta \in [0, 1]$), as function of the radius r for different dimensionless **BH** spin signed on the curves. Right panel: curves $\sigma_{\pm} = \text{constant}$ in the plane $r/M - a/M$. Radii $r_{\gamma}^{\pm}(a)$, counter-rotating and co-rotating photon circular orbits respectively on the equatorial plane, and boundary of the photon sphere radius are also shown (red curves). On $r_{\gamma}^{\pm}(a)$ there is $\sigma_{\pm} = 1$.

a. On photons spheres and replicas

In general, replicas are defined as solutions of $\mathcal{L}_{\mathcal{N}} = 0$ for $\omega = \text{constant}$ or, as in this work, for $\ell = \text{constant}$. Here, we look for special horizons replicas which are photon orbits with $\ell = \pm \ell_H^{\pm}$ solutions of (\mathfrak{R}) . Said differently, we consider special solutions of (\mathfrak{R}) , providing the luminous edge of the **BH** shadow, constrained by the conditions $\ell = \pm \ell_H^{\pm}$. For fixed a and σ , these solutions are points on the shadow profile.

Not all the horizons replicas can form the luminous textures of the shadow profile (i.e. they are not solutions of (\mathfrak{R})), and not all the solutions of (\mathfrak{R}) are horizons replicas. Constraints for the replicas on the shadow profile are given in details in Sec. (IV). (As discussed on Eq. (11) photon circular orbit $r_{\gamma} = 3M$ on the Schwarzschild spacetime is for example a solution of (\mathfrak{R}) , but it is easy to infer this is not a replica—see also discussion in Sec. (A 2).)

A photon shell or sphere is a region (spherical shell) of unstable bound photon orbits surrounding the central **BH**, it is the region $[r_{\gamma}^{-}, r_{\gamma}^{+}]$ with $\sigma \in [\sigma_{-}, \sigma_{+}]$, where σ_{\pm} are functions of (a, r) and $\phi \in [0, 2\pi[$, containing bound null geodesics. The boundary $r_{\gamma}^{\pm}(a)$ are the counter-rotating and co-rotating circular photon orbits located on the equatorial plane $\theta = \pi/2$ ($\sigma = 1$). Their explicit form is well known and can be found for example in [47]. (In particular for Schwarzschild spacetime, the photon shell is the two-dimensional sphere located at $r_{\gamma}^{\pm} = 3M$.) The limiting angles are

$$\sigma_{\pm} \equiv 1 - \cos^2 \theta_{\pm} \quad \text{where} \quad \cos^2 \theta_{\pm} \equiv \frac{r \left[2\sqrt{\Delta} [a^2 + r^2(2r - 3)] - (2a^2 + r(r^2 - 3)) \right]}{a^2(r - 1)^2}, \quad (\text{A5})$$

([47, 97])— see Figs (12)¹⁹.

The bound geodesics are unstable and after perturbation can fall into the **BH** or escape to infinity. Hence, the luminous edge, solutions of (\mathfrak{R}) in Eq. (10), is generated by nearly bound null geodesics on the observer screen— [18]. All the bound null geodesics lie in the photon sphere. Definition of **MBs** does not coincide with the photon shell, nor contain necessarily orbits of the photons sphere, as explained in details in Sec. (A 2). First a **MB** is defined as the couple $(a\sqrt{\sigma}, r)$, solutions of $\mathcal{L}_{\mathcal{N}} = 0$ for fixed ℓ (hence from normalization condition and the motion symmetries). In the representation of the extended plane **MBs** consider the collection of the spacetimes (for all spin $a > 0$, even $a > M$ for **NSs** spacetimes) where there is a solution of $\mathcal{L}_{\mathcal{N}} = 0$ for a fixed value of ℓ (see Figs.(11)). Not all the solutions of $\mathcal{L}_{\mathcal{N}} = 0$ are bound orbits (for example horizons and origin i.e. $r = 0$). Some replicas are solutions of Eq. (10) for certain spins and angles in accordance with the constraints of Sec. (IV), resulting in points on the luminous edge of the **BH** shadow. These special replicas are obtained by solving the system (\mathfrak{R}) with $\ell = \pm \ell_H^{\pm}(a)$.

¹⁹ We can consider the coordinates (r, σ) , discussed in Sec. (IV), for replicas solutions of (\mathfrak{R}) , with the locations of the photon shells, that is Figs (12).

b. *On circular photons orbits and replicas*

Let us concentrate on the Kerr equatorial plane. Among the all possible orbits of all bundles on $\theta = \pi/2$, there are the well-known geodesic photon circular orbits (which are also the geodesic marginally circular orbits). These orbits are special bundle orbits (but not necessary the **BH** horizons replicas of the **BH** tangent horizon), defined on the special bundle at $\sigma = 1$ having the characteristic frequency $\omega = 1/\ell_\gamma^\pm$, where $\ell_\gamma^\pm \equiv \ell(r_\gamma^\pm)$ is the photon conserved specific angular momentum ℓ given in Eq. (5) of the counter-rotating and co-rotating photon orbits r_γ^\pm , respectively. These orbits are also special points of the light surfaces bounding the stationary observer orbits. In Figs (11), we illustrate in detail the relation between (geodesic) photon circular orbits on the equatorial plane r_γ^\pm , metric bundles, replicas (left panel) and light surfaces (right panel).

Figure (11)–left panel– shows the bundles in the extended plane $a - r$. Solid curves are the (equatorial) co-rotating bundles, dashed curves are the counter-rotating bundles. Figure (11)–right panel– shows the light surfaces $r(\omega)$ as functions of the bundles characteristic frequencies ω (limiting photon circular frequencies of the stationary observers) on the equatorial plane for different **BH** spins. The case $a = 0$, corresponding to the Schwarzschild **BH** spacetime, is represented with black curves, and the Kerr **BH** with $a = \pm 0.999$ with blue curves. Bundles with characteristic frequency ω and angular momentum $\ell = 1/\omega = a_0 = \text{constant}$ (a_0 is the bundle origin spin at $r = 0$) are shown for different values of ℓ , signed on each curve. The radii r_γ^\pm are also represented. The points correspond to equatorial photon circular orbits (marginally circular orbits) of the spacetime. On the extended plane, a horizontal line represents a fixed spacetime $a = \text{constant}$. For $a = 0$, it is $\ell_\gamma^\pm = \mp 3\sqrt{3}$ on the orbits $r_\gamma^\pm = 3$. For $a = 0.999$, it is $\ell_\gamma^+ = -6.99833$ and $\ell_\gamma^- = 2.07813$, with $r_\gamma^- = 1.05208$ and $r_\gamma^+ = 3.99911$, respectively. It is clear that these orbits are not horizon replicas.

In this sense, we can read metric bundles as a generalization of these null (equatorial geodesic) circular orbits, included in the bundles as special points. Then marginally circular orbits that exist on the equatorial plane of the Kerr or Schwarzschild spacetimes are, in general, *not* horizon replicas of the Schwarzschild **BH** and the Kerr **BH** with $a = \pm 0.999$, respectively.

Appendix B: Further notes on the shadow analysis

The functions r_H^\pm , introduced in Sec. (IV A) can be found as a zero of the quantity:

$$R_H^+ \equiv a^4 + (2a^2 + 5)r^4 + 4(4 - a^2)r^3 + 8a^2 + (a^4 - 6a^2 - 12)r^2 + 2a^2(a^2 - 4)r + r^6 - 6r^5. \quad (\text{B1})$$

Radius r_H^+ can be found also as solution of $a(r) = \bar{a}_H^+ = \bar{a}_+^-$, where

$$\bar{a}_\mp^\pm \equiv \sqrt{\frac{r[4 - (r - 3)r(r + 1)] \mp 2 \left[\sqrt{(r - 1)^3(r[(r - 1)r - 4] - 4)} \pm 2 \right]}{(r + 1)^2}}, \quad (\text{B2})$$

while r_H^- can be also found as solution of $a = a_H^-(r) \equiv \bar{a}_{\mp}^\pm$ -Figs (2). Limiting plane σ_ω^+ , shown in Figs (3)-right panel, can be found as a solution of the equation

$$\sum_{i=0}^{12} n_i \sigma^i = 0 \quad \text{where} \quad (\text{B3})$$

$$\begin{aligned} n_0 &\equiv 4096a^2 (a^2 - 1)^2, \\ n_1 &\equiv 2048(a^2 - 1) (a^6 + 16a^4 - 87a^2 + 54), \\ n_2 &\equiv 256 (a^{10} + 220a^8 - 466a^6 + 972a^4 + 1257a^2 - 1728), \\ n_3 &\equiv 512 (41a^{10} + 431a^8 - 823a^6 - 5155a^4 + 4754a^2 - 1296), \\ n_4 &\equiv 256 (9a^{12} + 577a^{10} - 5232a^8 + 18447a^6 + 961a^4 + 3606a^2 - 1728), \\ n_5 &\equiv 256 (98a^{12} - 2083a^{10} + 10317a^8 - 20461a^6 + 6741a^4 + 2748a^2 - 432), \\ n_6 &\equiv 32a^2 (35a^{12} - 2804a^{10} + 19730a^8 - 69292a^6 + 64139a^4 + 51992a^2 + 2504), \\ n_7 &\equiv -64a^4 (72a^{10} - 1541a^8 + 6823a^6 - 8371a^4 + 14253a^2 - 8164), \\ n_8 &\equiv 16a^6 (9a^{10} + 417a^8 - 2288a^6 + 13455a^4 + 4481a^2 + 566), \\ n_9 &\equiv -8a^8 (45a^8 + 497a^6 - 29a^4 + 5507a^2 - 3972), \\ n_{10} &\equiv a^{10} (a^8 + 284a^6 + 686a^4 + 204a^2 - 919), \\ n_{11} &\equiv -2a^{12} (a^6 + 33a^4 - 53a^2 + 19), \\ n_{12} &\equiv a^{14} (a^2 - 1)^2, \end{aligned}$$

(see also [36]). Radius $\bar{r}_H^-(a)$, discussed in Sec. (IV A)m can be found as a solution of the which is a zero of the quantity \bar{R}_H^- :

$$\bar{R}_H^- \equiv a^2 + 2(a^2 - 3)r + (a^2 + 5)r^2 - 4r^3 + r^4. \quad (\text{B4})$$

Alternately $\bar{r}_H^-(a)$ can be expressed by the spin function \bar{a}_H^- :

$$\bar{a}_H^- \equiv \sqrt{-\frac{(r-3)r[(r-1)r+2]}{(r+1)^2}} \quad (\text{B5})$$

(dotted-dashed curve of Figs (2)), where $\bar{r}_H^-(a)$ is a solution of $a = \bar{a}_H^-(r)$.

-
- [1] K. Akiyama et al. (Event Horizon Telescope), *Astrophys. J.* 875, L1 (2019).
 - [2] K. Akiyama et al. (Event Horizon Telescope), *Astrophys. J.* 875, L4 (2019).
 - [3] K. Akiyama et al. (Event Horizon Telescope), *Astrophys. J.*, 875, L3 (2019).
 - [4] K. Akiyama et al. (Event Horizon Telescope), *Astrophys. J.*, 875, L4 (2019).
 - [5] K. Akiyama et al. (Event Horizon Telescope), *Astrophys. J.*, 875, L5 (2019).
 - [6] K. Akiyama et al. (Event Horizon Telescope), *Astrophys. J.*, 875, L6 (2019).
 - [7] K. Akiyama et al. (Event Horizon Telescope), *ApJL*, 910, L12 (2021).
 - [8] K. Akiyama et al. (Event Horizon Telescope), *ApJL*, 910, L13 (2021).
 - [9] L. Medeiros, et al., *ApJL*, 947, L7 (2023).
 - [10] K. Akiyama et al. (Event Horizon Telescope), *ApJL*, 930, L12 (2022).
 - [11] K. Akiyama et al. (Event Horizon Telescope), *ApJL*, 930, L13 (2022).
 - [12] K. Akiyama et al. (Event Horizon Telescope), *ApJL*, 930, L14 (2022).
 - [13] K. Akiyama et al. (Event Horizon Telescope), *ApJL*, 930, L15 (2022).
 - [14] K. Akiyama et al. (Event Horizon Telescope), *ApJL*, 930, L16 (2022).
 - [15] K. Akiyama et al. (Event Horizon Telescope), *ApJL*, 930, L17 (2022).
 - [16] J. L. Synge, *Mon. Not. R. Astron. Soc.* 131, 463 (1966).
 - [17] J. P. Luminet, *Astron. Astrophys.* 75, 228 (1979).
 - [18] J. M. Bardeen, in *Black Holes*, edited by C. Dewitt and B. S. Dewitt (CRC, Boca Raton, FL, 1973).
 - [19] S. Chandrasekhar, *The Mathematical Theory of Black Holes*; Oxford Classic Texts in the Physical Sciences; Oxford University Press: Oxford, UK, (2002).

- [20] F. Tamburini, et al. MNRAS: Letters. 492: L22–L27 (2020).
- [21] K. Hioki and K. Maeda, Phys. Rev. D, 80, 024042, (2009).
- [22] T. Johannsen, Astrophys. J. 777, 170 (2013).
- [23] M. Ghasemi-Nodehi, Z.-L. Li, and C. Bambi, Eur. Phys. J. C 75, 315 (2015).
- [24] A. A. Abdujabbarov, L. Rezzolla, and B. J. Ahmedov, Mon. Not. Roy. Astron. Soc. 454, 2423 (2015).
- [25] H. Falcke, F. Melia, and E. Agol, Astrophys. J. 528, L13 (2000).
- [26] R. Takahashi. Astrophys. J. 611, 996 (2004).
- [27] K. Beckwith and C. Done, Mon. Not. R. Astron. Soc. 359, 1217 (2005).
- [28] A. E. Broderick and A. Loeb, Astrophys. J. 636, L109 (2006).
- [29] A. E. Broderick and R. Narayan, Astrophys. J. 638, L21 (2006).
- [30] L. Huang, M. Cai, Z. Q. Shen, and F. Yuan, Mon. Not. R. Astron. Soc. 379, 833 (2007).
- [31] V. I. Dokuchaev, and N. O. Nazarova, Physics-Uspekhi 63 (6) 583, (2020).
- [32] D. Pugliese and H. Quevedo, Eur.Phys.J. C 81 3, 258 (2021).
- [33] D. Pugliese and H. Quevedo, Eur. Phys. J. C 79, 3, 209 (2019).
- [34] D. Pugliese and H. Quevedo, Eur. Phys. J. C 82, 12, 1090 (2022).
- [35] D. Pugliese and H. Quevedo, Eur. Phys. J. C 82, 5, 456 (2022).
- [36] D. Pugliese and H. Quevedo, Nucl. Phys. B 972, 115544 (2021).
- [37] D. Pugliese and H. Quevedo, Gen. Rel. Grav. 53, 10, 89 (2021).
- [38] D. Pugliese and H. Quevedo, Eur. Phys. J. C 81 3, 258 (2021).
- [39] R.S. Lu, K. Asada, T.P. Krichbaum, et al, Nature 616, 686–690 (2023).
- [40] B. Crinquand, B. Cerutti, G. Dubus, K. Parfrey, and A. Philippov, Phys. Rev. Lett., 129, 205101 (2022).
- [41] W. Lockhart, S. E. Gralla, MNRAS, 517, 2462 (2022).
- [42] D.C. M. Palumbo and G. N. Wong, ApJ, 929, 49 (2022).
- [43] A. E. Broderick, et al., ApJ, 935, 61 (2022).
- [44] A. E. Broderick, et al., ApJ, 927, 6 (2022).
- [45] M. Wielgus et al., ApJL, 930, L19 (2022).
- [46] P. Tiede, A. E. Broderick, D. C. M. Palumbo, A. Chael, ApJ, 940, 182 (2022).
- [47] M. D. Johnson et al., Sci. Adv., 6,12 (2020).
- [48] W. Lockhart and S. E. Gralla, MNRAS, 509, 3643–3659 (2022).
- [49] E. Papoutsis, M. Bauböck, D. Chang, C. F. Gammie, ApJ, 944, 55 (2023).
- [50] B. Carter, Phys. Rev., 174, 1559, (1968).
- [51] F. de Felice, Mont. Notice R. astr. Soc 252 197-202 (1991).
- [52] F. de Felice, Class. Quantum Grav. 11, 1283-1292 (1994).
- [53] F. de Felice and S. Usseglio-Tomasset, Gen. Rel. Grav. 28, 2 (1996).
- [54] F. de Felice and S. Usseglio-Tomasset, Gen. Rel. Grav. 24, 10 (1992).
- [55] F. de Felice and Y. Yunqiang, Class. Quantum Grav. 10, 353-364 (1993).
- [56] F. de Felice and L. Di G. Sigalotti, Ap.J. 389, 386-391 (1992).
- [57] F. de Felice and S. Usseglio-Tomasset, Class. Quantum Grav. 8., 1871-1880 (1991).
- [58] C. Chakraborty, P. Kocherlakota, M. Patil, et al. Phys. Rev. D, 95, 084024, (2017).
- [59] I. V. Tanatarov and O. B. Zaslavskii, Gen. Rel. Grav. 49, 9, 119 (2017).
- [60] S. Mukherjee and R. K. Nayak, Astrophys. Space Sci. 363, 8, 163 (2018).
- [61] O. B. Zaslavskii., Phys. Rev. D 98, 10, 104030 (2018).
- [62] C. S. Reynolds, Ann. Rev. Astron. Astrophys. 59, 117-154 (2021).
- [63] R. Abbott *et al.* [LIGO Scientific, VIRGO and KAGRA], [arXiv:2111.03606 [gr-qc]].
- [64] C. J. White, J. Dexter, O. Blaes, E. Quataert, ApJ, 894, 14 (2020).
- [65] O. Porth, K. Chatterjee, R. Narayan, et al., ApJS, 243, 26 (2019).
- [66] M. Janssen et al. Nature Astronomy. 5 (10): 1017–1028 (2021).
- [67] K. Chatterjee, Z. Younsi, M. Liska et al., MNRAS, 499, 362–378 (2020).
- [68] R. Emami et al., Astrophys. J., 923, 272 (2021).
- [69] M. Lucchini, F. Kraub, S. Markoff, MNRAS, 489, 1633 (2019).
- [70] F. H. Vincent, et al., A&A 624, A52 (2019).
- [71] B. Curd, R. Emami, R. Anantua, et al. MNRAS, 519, 2812 (2023).
- [72] R. Anantua, et al. Galaxies, 11, 4 (2023).
- [73] S. E. Gralla, D. E. Holz, & R. M. Wald, Phys. Rev. D, 100, 024018 (2019).
- [74] S. E. Gralla, & A. Lupsasca, Phys. Rev. D, 101, 044031 (2020).
- [75] R. Narayan, M. D. Johnson, & C. F. Gammie, ApJ, 885, L33 (2019).
- [76] B. Punnsly, Black Hole Gravitohydromagnetics, Springer–Verlag Berlin Heidelberg (2009).
- [77] M. Camenzind, Compact Objects in Astrophysics: White Dwarfs, Neutron Stars and Black Holes, Springer Berlin, Heidelberg (2007).
- [78] R. D. Blandford and R. L. Znajek, MNRAS, 179, 433–456, (1977).
- [79] R. L. Znajek, MNRAS, 179, 457, (1977).
- [80] H-Y. Pu, M. Nakamura, K. Hirotani, Y. Mizuno, K. Wu, and K. Asada, Astrophys. J., 801:56, (2015).
- [81] D. A. Uzdensky, Astrophys. J., 603:652–662, (2004).
- [82] A. Tchekhovskoy, R. Narayan, and J. C. McKinney, Astrophys. J., 711, 50–63, (2010).

- [83] Z. Pan, *Phys. Rev. D*, 98, 043023 (2018).
- [84] S. S. Komissarov, *MNRAS*, 350, 427–448 (2004).
- [85] D. A. Uzdensky *Astrophys. J.*, 620:889–904, (2005).
- [86] J. F. Mahlmann, P. Cerda–Duran, M. A. Aloy, *MNRAS*, 477, 3, 3927–3944 (2018).
- [87] D. A. Macdonald, *MNRAS*, 211, 313–329 (1984).
- [88] S. S. Komissarov, J. C. McKinney, *MNRAS*, 377, L49–L53 (2007).
- [89] J. C. McKinney, *MNRAS*, 368, 1561–1582 (2006).
- [90] B. Crinquand, B. Cerutti, G. Dubus, K. Parfrey, and A. Philippov, *A&A* 650, A163 (2021).
- [91] I. Contopoulos, D. Kazanas and C. Fendt, *Astrophys. J.*, 511, 351–358, (1999).
- [92] I. Contopoulos, D. Kazanas, and D. B. Papadopoulos, *Astrophys. J.*, 765, 113 (2013).
- [93] J. C. McKinney, and R. Narayan, *MNRAS*, 375, 531–547 (2007).
- [94] A. Nathanail, and I. Contopoulos., *Astrophys. J.*, 788,186, (2014).
- [95] A. Chael, M. D. Johnson, and A. Lupsasca, *ApJ*, 918, 6, 2021
- [96] V. Perlick, *Living Rev. Relativ.* 7, 9 (2004).
- [97] H. Yang, *Physical Review D* 86, 104006 (2012).